Land Cover Classification using Sentinel-1 Radar Mission Interferometry

Muhammad Arsalan-Ul-Haque

School of Electrical Engineering

Thesis submitted for examination for the degree of Master of Science in Technology.

Espoo 20.08.2017

Thesis supervisor:

Prof. Jaan Praks

Thesis advisor:

D.Sc. (Tech.) Oleg Antropov

Aalto University
School of Electrical
Engineering

AALTO UNIVERSITY
SCHOOL OF ELECTRICAL ENGINEERING

ABSTRACT OF THE
MASTER'S THESIS

Author: Muhammad Arsalan-Ul-Haque

Title: Land Cover Classification using Sentinel-1 Radar Mission Interferometry

Date: 20.08.2017 Language: English Number of pages: 11+69

Department of Electronics and Nanoengineering

Professorship: Space Science and Technology (S-92)

Supervisor: Prof. Jaan Praks

Advisor: D.Sc. (Tech.) Oleg Antropov

Synthetic Aperture Radar (SAR) has been widely used for many years in the field of remote sensing. SAR has valuable contribution due to its ability to provide complementary information to optical systems, penetration of radar waves through volumetric targets and high-resolution. SAR has the ability to operate during day and night. It provides operational services under all weather conditions. SAR imagery has many applications including land cover changes, environmental monitoring, climate change and military surveillance.

This work focuses on land cover classification with SAR interferometry (InSAR) technique using Sentinel-1 space radar image pair. Sentinel-1 data were collected over the southern part of Estonia. Two SLC SAR images were acquired from both Sentinel-1A and Sentinel-1B with six days temporal difference. In this study, interferometric coherence and backscattering intensity processing chains have been set up and applied to Sentinel-1 SAR image pair. The Sentinel Application Platform (SNAP) has been used for processing of single pair for Sentinel-1 mission. The SNAP is an European Space Agency (ESA) software. The Sentinel-1 image pair processing has been done using Sentinel-1 Toolbox (S1TBX) which is a part of SNAP. Corine Land Cover (CLC) 2012 database has been used as a reference data with 20 m resolution. The CLC2012 contains land use/cover information for most of the European countries. A single optical image from Sentinel-2A was additionally used for feature extraction. An overall accuracy of 68% to 73% was achieved when performing classification into five classes (*Urban*, *Field*, *Forest*, *Peat-land*, *Water*) using supervised classification with k-nearest neighbour (kNN) algorithm. The accuracy assessment was done by using confusion matrices.

Keywords: synthetic aperture radar, SAR, remote sensing, land cover classification, SAR interferometry, InSAR, interferometric coherence, backscattering intensity.

Acknowledgements

The research and report writing has been carried out in the department of Electronics and Nanoengineering of Aalto University over the period of six months from March to August, 2017.

I would first like to express my gratitude to my thesis supervisor Prof. Jaan Praks, Professor in Aalto University, for employing me and giving an opportunity to be part of his research group and carrying out my diploma work under his supervision. He has always been a great support through the learning process and his office door was always opened whenever I had any trouble about research or thesis writing.

Secondly, I want to thank my thesis advisor Dr. Oleg Antropov, Post-Doctoral Researcher in Aalto University, for his guidance and encouragement during the thesis. I am grateful for having him as my advisor and the scientific discussions I had with him were invaluable for the completion of my research work within specified time period.

Finally, I express my gratitude to my parents and friends for being an unfailing support and encouragement throughout my years of study, and especially while making decision to pursue my studies abroad. This achievement would not have been possible without them. Thank you.

Otaniemi, 20.08.2017

Muhammad Arsalan-Ul-Haque

Contents

List of Symbols

a	Azimuth coordinate in SAR image
A	Amplitude
B_n	Perpendicular baseline
c	speed of light in vacuum $\approx 3 \times 10^8$ [m/s]
G	Gain of antenna
h_a	Height of ambiguity
h	Height of surface variation
I	Intensity (power)
L	Length of radar antenna
P_r	Received power
P_t	Transmitted power
q	Altitude difference between targets
q_s	Displacement between the resolution cells
r	Range coordinate in SAR image
R_a	Azimuth resolution
R_r	Range resolution
R	Range
s	Slant range displacement of targets
t	Propagation time
$\overline{Z}$	Complex SAR image
β_o	Estimated backscattered power
δr	Slant range
$\Delta\phi$	Interferometric phase variation
Δr	Travel path difference
γ	Complex interferometric coherence
ϕ	Phase
λ	Wavelength
θ	Look angle
θ_i	Incidence angle
$\theta_{i,local}$	Local incidence angle
σ	Radar cross section
σ^o	Radar backscattering coefficient
τ	Pulse length

List of Abbreviations

ATI	Along Track Interferometry
CLC	Corine Land Cover
CRS	Coordinate Reference System
CSA	Chirp Scaling Algorithm
DEM	Digital Elevation Model
DN	Digital Number
EEA	European Economic Area
EMS	Electromagnetic Spectrum
EO	Earth Observation
EPSG	European Petroleum Survey Group
ERS	European Remote Sensing Satellite
ESA	European Space Agency
EW	Extra Wide swath mode
FFT	Fast Fourier Transform
GPS	Global Positioning System
IFFT	Inverse Fast Fourier Transform
InSAR	SAR Interferometry
IW	Interferometric Wide swath mode
kNN	k-Nearest Neighbour
LEO	Low Earth Orbit
NASA	National Aeronautics and Space Administration
NIR	Near Infrared
PNN	Probabilistic Neural Network
PolSAR	Polarimetric SAR
PRF	Pulse Repetition Frequency
QGIS	Quantum Geographic Information System
RADAR	Radio Detection and Ranging
RCMC	Range Cell Migration Correction
RDA	Range Doppler Algorithm
SAR	Synthetic Aperture Radar
SLC	Single Look Complex
SM	Stripmap mode
SNR	Signal to Noise Ratio
SRTM	Shuttle Radar Topography Mission
TIR	Thermal Infrared
TOPSAR	Terrain Observation with Progressive Scanning SAR
USGS	U.S. Geological Survey
UTM	Universal Transverse Mercator
WV	Wave mode
XTI	Cross Track Interferometry

List of Figures

List of Tables

1 Introduction

Land cover and land use describe physical appearance of the surface of Earth over a specific area. These two terms are often used interchangeably, and therefore, they need to be defined comprehensively. Land cover is a representation of observed physical cover of the Earth surface containing various classes such as built-up areas, agricultural areas, forests, wetlands and water bodies [1]. On the other hand, land use is a representation of present and future activities by humans on land [2, 3], identified as industrial, commercial, forestry and leisure. Land cover/use information is of great importance for scientific research and applications. Land cover plays a vital role in the geographical analysis ranging from the study of earth sciences to environmental analysis. Land cover maps need to be updated regularly, as they act as a catalyst between socio-economic activities and regional environmental changes. Land cover classification is an important application of remote sensing. Past studies have investigated the efficient usage of remote sensing data for both local and global scale thematic characterization [4]. Moreover, remotely sensed images can be used for consistent and continuous monitoring of Earth's surface to identify the changes in land cover over large areas [5]. In many studies [6, 7, 8], SAR data has been investigated and proven effective for land cover monitoring.

Technological breakthroughs in remote sensing enable us to monitor dynamics of the Earth surface. Precise and reliable information is required to detect the land change and monitoring of the area of interest. Over the past few years, many optical and Synthetic Aperture Radar (SAR) satellite missions have been launched. During the period 2013-2016, European based Copernicus programme successfully launched Sentinel-1 [9], and Sentinel-2 constellations. Landsat-8 mission was launched as a collaboration between the U.S. Geological Survey (USGS) and the National Aeronautics and Space Administration (NASA) [10] with high spatial resolution (10-30 m). Sentinel missions data are available on Sentinels data hub, under the management of the European Space Agency (ESA) and is free to use for scientific and technological purposes.

Nowadays, optical imagery is often used for land cover classification. The optical sensors can not operate during night and cloud cover restrict its operability in many areas of the Earth. However, SAR sensor is capable of working almost under all weather conditions and can penetrate through cloud cover. Microwave frequency band of SAR system spans over different wavelengths. The penetration of radar wave depends on chosen wavelength. For example, P-Band has 1 m wavelength and its penetration through surface targets is high as compared to other frequency bands. The decrease in wavelength effects radar wave penetration through the target. The Sentinel-1 radar mission is operating at C-band. The penetration capability of C-band is less than P-band. SAR has restrictions regarding the potential of C-band single polarization intensity images [8]. These limitations can be avoided with InSAR technique. Interferometric SAR (InSAR) enhances the potential usage of backscattering intensity by using interferometric coherence as a complementray information [11]. This study mainly focuses on land cover mapping using InSAR technique.

1.1 Remote Sensing

Remote sensing is the science of collecting information by a remote device which is not in direct contact with the object under investigation [12]. In simple words, spaceborne remote sensing can also be defined as observing the planet Earth from space.

Remote sensing satellites acquire Earth surface imagery from orbit. Data acquisition by satellite sensor is done in different wavelength regions of Electromagnetic Spectrum (EMS). The optical remote sensing uses passive instruments which depend on radiated or reflected energy. The EMS for optical remote sensing spans over visible to near infrared (NIR) up to thermal infrared (TIR) region. However, radar is an active imaging sensor and it uses microwave region of EMS. In the EMS, the selected wavelength region plays an important role for a remotely sensed image. Some of the remotely sensed images represent the reflection of solar energy in the visible and the near infrared regions. However, some are the measurements of the energy emitted by the Earth surface itself in the thermal infrared wavelength region. Microwave remote sensing uses active and passive sensors. In active microwave systems, the remote sensing platform itself is the source of the emitted energy [13], whereas passive microwave sensors depends on external energy source such as Sun.

1.2 InSAR Studies on Land Cover

The topic of this thesis is *"Land Cover Classification using Sentinel-1 Radar Mission Interferometry"*. Sentinel-1 constellation has many operational applications and land cover mapping is one of them. Many studies have already been conducted in land cover mapping using SAR based European missions including ERS-1/2, Envisat, and sentinel-1A. With the launch of Sentinel-1B on April 25, 2016, the Sentinel-1 constellation is complete and operating successfully with 24/7 global coverage. Some of the areas in which remote sensing imagery has many applications include land cover mapping, agriculture, environmental monitoring, Earth-resource mapping, water resource management, disaster monitoring and mitigation, soil mapping, forestry, survey and urban planning, military observations and land cover changes [14].

Previously encouraging results have been achieved using European Remote Sensing (ERS) satellite datasets and different classification methods. Dammert et al. performed classification research in two areas of Sweden. Classification accuracy of 65% to 75% was achieved in Gothenburg into five classes, while for Hokmark it was between 60% and 65% [15]. Dammert used unsupervised segmentation method on multiple Tandem pairs for classification. Strozzi et al. conducted research on three different test sites including Bern, Lozère and Tuusula. Strozzi et al. used both supervised and unsupervised classification algorithms on multiple Tandem pairs and achieved 75% classification accuracy into four classes[16]. Forest/nonforest—classification accuracy of 80% to 85% was achieved. Engdahl et al. achieved an overall classification accuracy for Helsinki metropolitan area was of 90% into six classes with a kappa coefficient of 0.86 [17]. Engdahl used the ERS-1/2 tandem InSAR datasets and two-stage hybrid classifier method for land cover classification. Although, they all

used multiple Tandem pairs but the classification techniques are same as used in this thesis.

1.3 Motivation

The goal for this study is to investigate the usage of interferometric SAR coherence in combination with backscattering intensity using Sentinel-1 image pair with six days temporal baseline. The work presented in this study focuses on the potential of single pair C-band InSAR data for Sentinel-1 mission in land cover monitoring. The main questions to be answered here are:

1. Will it be possible to achieve results for land cover classification with the Sentinel-1A/B interferometric dataset?

2. Can the interferometric coherence be used with intensity parameter to improve land cover classification?

3. How temporal decorrelation affect land cover classification results?

The supervised classification algorithm is used in order to answer the above mentioned questions. The potential of single pair C-band InSAR data of Sentinel-1 is investigated for land cover mapping using Interferometric Wide (IW) swath mode. The IW mode is the main operational mode over land for Sentinel-1 and it contains an abundance of information relating to land cover monitoring.

1.4 Structure of the Report

The thesis is divided into six chapters. Chapter 1 presents the general discussion about the topic, motivation, research problem and thesis goal. In chapter 2, theory and technical parameters of the SAR interferometry is discussed. The chapter 3 presents the material used for this work. Chapter 4 explains the research methodology containing processing chains of interferometric coherence, backscattering and Corine land cover model. In chapter 5, the results are given with the analysis. Chapter 6 gives the conclusion and future recommendations.

2 Theoretical Background

This chapter covers the theoretical background of the thesis. The chapter has three sections. Section 2.1 explains the basic theory in understanding the working principles and properties of Synthetic Aperture Radar (SAR). Section 2.2 gives necessary concepts for better understanding of SAR interferometry (InSAR). Section 2.3 present the methods and techniques used for land cover classification. Mostly, the literature review is based on [12, 13, 20].

2.1 Overview of Radar and SAR

The term *Radar* stands for Radio Detection and Ranging. A radar is an object detection system that measures the distance (range), angle or velocity to an object. The electromagnetic signals are transmitted to the ground from radar and reflected echo is received from the target. A radar system consists of a transmitter, receiver, transmitting and receiving antennas and processor to process the received echoes shown in Fig.1.

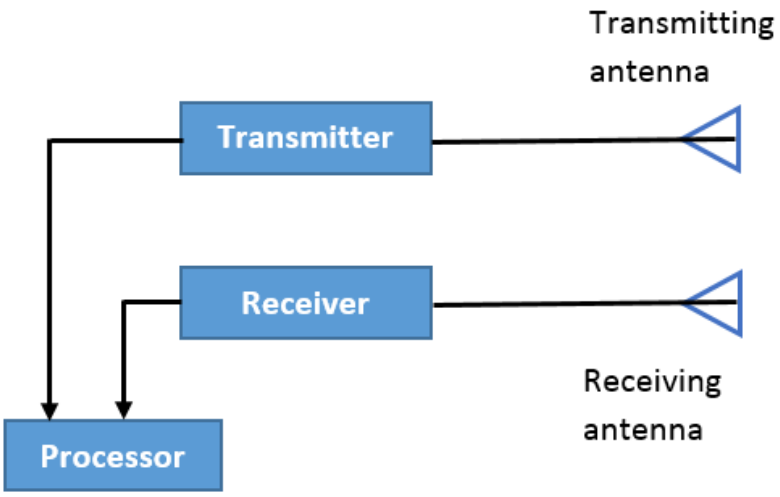

Figure 1: Elements of radar system.

Range or distance to the target can be calculated by measuring the time it takes the electromagnetic signal to propagate to the object and back to the receiver. The electromagnetic signal travels at the speed of light. The signal travels from transmitting antenna to the object and then propagates back to the receiving antenna after reflecting from the object. The electromagnetic signal travels twice the distance between the radar and ground target [13]. Therefore, the range (R) can be calculated as

$$R = \frac{1}{2}ct, \tag{1}$$

where c is the speed of light in vacuum, $\frac{1}{2}$ indicates that the radar signal travelled twice the distance measured since the signal first travels from the transmitter to the target and then from target to the receiver and t is the propagation time.

Radar is an active remote sensing instrument. It has its own source of energy. It does not depend on ambient radiation like optical and infrared sensors. Radar can detect and measure the range of relatively small objects at near or far range with precision during day or night. Imaging remote sensing radars, such as SAR, produce high-resolution images of Earth surface. They provide geophysical information by using post-processing techniques on high resolution images. SAR uses backscattered echoes to gather surface information and produce high resolution images [13].

SAR is a side looking microwave imaging system. Remote senisng techniques have been using SAR system for more than 30 years. Being an active system and usage of microwaves enhance its operational capabilities. To acheive the accurate measurements of radiation travel path, interferometric method is useful in SAR systems. The travel path variations in imaging radars can be measured by using satellite position and acquitsition time, which is helpful in generating digital elevation models (DEM) [18].

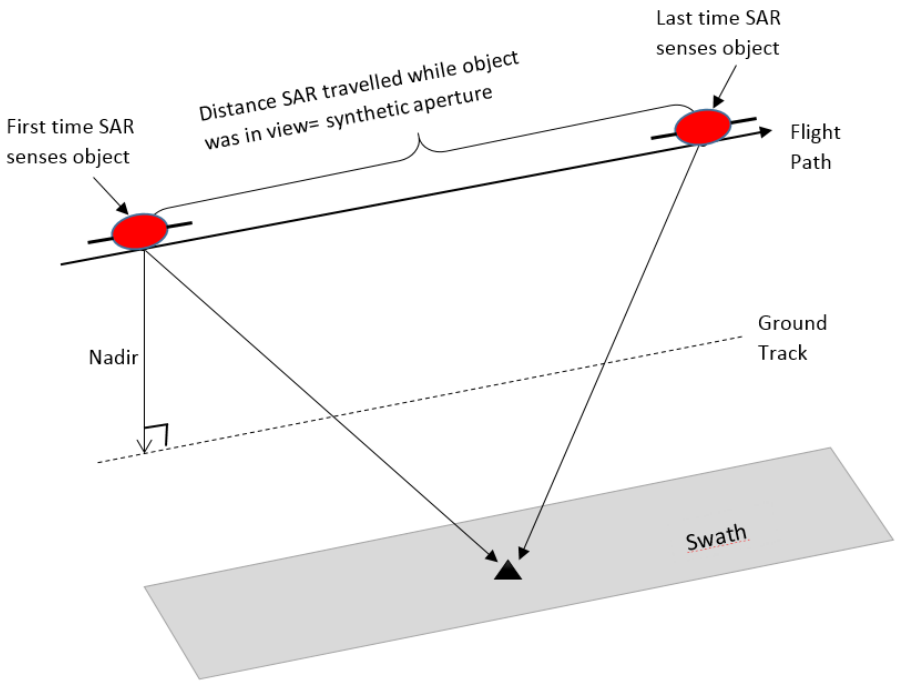

Figure 2: Spaceborne SAR measures distance between spacecraft and the object along the direction of flight.

The principle of SAR instruments is similar to conventional radar. Radar transmit electromagnetic waves and measure the intensity of backscattered echoes by the radar antenna mounted on a moving platform. The time it takes the electromagnetic signal to reach the target and received back at the antenna tells how far is the target from the SAR platform. The SAR measures the distance between the satellite and the ground targets in the direction of flight shown in Fig.2. The radar has a restriction

to the physical length of the antenna mounted on a moving platform. In SAR, the resolution in azimuth is proportional to the size of the antenna. In order to achieve better resolution in azimuth, the physical size of the antenna needs to be increased which is often not practically possible. Moreover, shortening the wavelength will limit its penetration through the cloud cover. To overcome these limitations, SAR uses doppler history of the backscattered echoes. Forward motion of SAR platform generates backscattered echoes which synthesizes a large antenna. Thus, it becomes possible to acquire high resolution image irrespective of small size of physical antenna.

SAR technology has various applications. It provide terrain structural information to geologists for mineral exploration, oil spill boundaries on water to environmentalists, sea state and ice hazard maps to navigators, and targeting information to military operations. SAR applications for civilian usage have not yet been adequately explored. The lower cost electronics are just beginning to make SAR technology economical for smaller scale uses [19].

2.1.1 Principles of Imaging Radar

SAR system is mounted on a moving platform and includes various components: a transmitter, a receiver, an antenna and a recorder. The transmitter generates electromagnetic signal and send the signal to the transmitting antenna. The antenna transmits the signal to ground surface. The receiver collects the backscattered energy as received by the receiving antenna, filters and amplifies for recording. Finally, the recorder then stores the received signal for post processing.

Image acquired by radar is presented in the form of pixels. Each pixel contain digital number which represents the intensity of the backscattered signal. This backscattered signal is received at the receiving antenna. Each transmitted pulse from radar carries energy which can be expressed by radar equation [20] as

$$P_r = \frac{G^2 \lambda^2 P_t \sigma}{(4\pi)^3 R^4}, \tag{2}$$

where P_r is the received power, λ is the wavelength, G is the gain of antenna, P_t is the transmitted power, σ is the radar cross section and R is the range from sensor to the target.

Some factors effecting the strength of the backscattered signal are:

- properties of radar system including wavelength, antenna and transmitted power,
- imaging geometry of radar defines the size of the illuminated area. The size depends on a beam-width, incidence angle and range,
- object characteristics in relation to the radar signal, i.e., surface roughness and composition, and terrain topography and orientation.

2.1.1.1 Radar System Measurements

Radar images require correct interpretation and therefore it is necessary to understand the working principle of radar and what it detects. The transmitter transmits microwave pulses at regular intervals, called Pulse Repetition Frequency (PRF) [20]. The PRF are bundled together by the antenna to form a beam. This beam travels through the atmosphere and illuminates a target. It is backscattered and travels through the atmosphere again to reach the antenna where the signal intensity is received. Knowing the speed of light and time interval; the signals needs to pass twice the distance between the object and antenna, the distance (range) between the sensor and object can be derived [20].

The signal is received at a receiver and sampling is performed on a signal pulse. These samples are stored in an image line to create an image. A 2D image is created as the pulses are emitted from the sensor that is mounted on a moving platform and each pulse defines one line. The radar sensor, therefore, measures distances and detects backscattered signal intensities.

2.1.1.2 Imaging Radar Frequency Bands

Imaging radar sensors operate with different frequency bands similarly to optical remote sensing. For better identification of the wavelength ranges, a standard has been established that uses letters to distinguish among the various bands. Radar missions uses different wavelengths depending on the application. The European Sentinel-1 mission uses C-band (freq: 5.405 GHz) radar. C-band has many land applications and it is also used for imaging oceans and ice features as well [21]. The different frequency bands in microwave spectrum are shown in Fig.3.

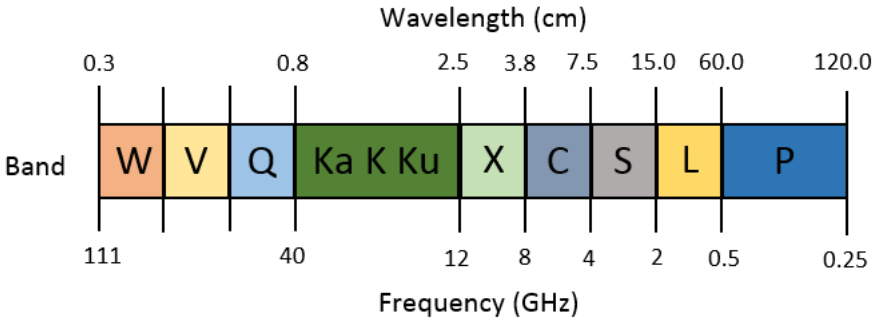

Figure 3: Microwave spectrum commonly used bands and their notation.

2.1.1.3 Microwave Polarizations

The microwave polarization is important in imaging radar systems. The polarization of radar imagery depends on the orientation of transmitted and received Electromagnetic Wave (EM). EM waves can be horizontal, vertical or cross polarized. Polarization is defined by the orientation of the electric field vector with respect to

horizontal direction. If the electric field vector oscillates parallel to the horizontal direction, the beam is referred to as horizontally polarized, otherwise vertically polarized shown in Fig.4. Information regarding different applications can be collected using different polarizations and wavelengths.

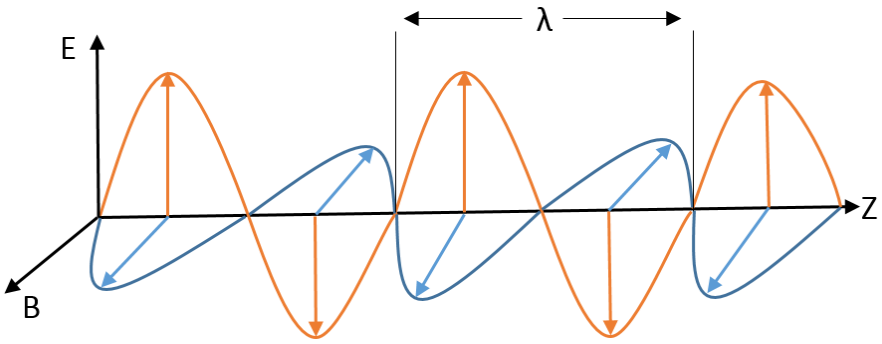

Figure 4: Vertically polarized electromagnetic wave of wavelength λ has electric field vector **E** (orange) in vertical direction. The magnetic field **B** (blue) is perpendicular to **E** and both are perpendicular to direction of propagation **Z**.

The backscattered energy can have a different polarization after reflecting from the object. The Sentinel-1 C-band SAR instrument has one switchable transmit chain and two parallel receive chains [22]. These chains operate in single (HH or VV) polarization as well as in dual (HH+HV or VV+VH) polarizations.

- **HH**: transmitting and receiving signal in horizontal polarization,
- **VV**: transmitting and receiving signal in vertical polarization,
- **HV**: transmit in horizontal and receive in vertical polarization, and
- **VH**: transmit in vertical and receive in horizontal polarization.

2.1.1.4 Incidence Angle

The incidence angle θ_i is defined as the angle between the incident radar beam and the direction normal to the Earth surface. The transmitted microwave energy has dependency on angle of incidence of radar pulse. In general, increasing the incidence angle will decrease the intensity of the received backscattering energy from the surface. The angular relationship between the incident radar beam and the surface layer or target is normally described by the angle of incidence [23] shown in Fig.5. Sentinel-1 operates in four acquisition modes [22] and each mode has a different incidence angle range. In this study, we focus on Interferometric wide (IW) swath mode.

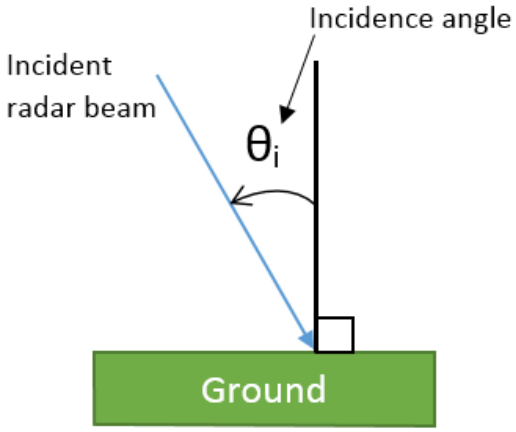

Figure 5: SAR incident angle.

2.1.2 Radar Backscattering Coefficient

Radar backscattering coefficient σ^o gives information about the surface roughness, moisture content in soil and vegetation cover. The coefficient can be described by comparing the backscattered power with the incident power on surface scatterers. The equation used for computing the radar backscattering coefficient of sensor is generally associated to the SAR image brightness as follows

$$\sigma^o = \frac{\beta_o}{sin\theta_i}, \tag{3}$$

where β_o is the radar brightness. The radar brightness is the estimated backscattered power from the ground target. The radar detects the backscattered power and measure in the slant-range geometry. The brightness does not depend on the incidence angle and the local topography [24]. The backscattering coefficient in decibels is given as

$$\sigma^o(dB) = 10log_{10}(\sigma^o), \tag{4}$$

where σ^o is the radar backscattering coefficient in decibels.

2.1.2.1 Parameters Affecting Radar Backscatter

The scattering of microwave radiation depends on geometrical and dielectric properties of natural land surface [25]. The ground scatterers including urban areas, forest and water exhibit different scattering features. The urban areas are very strong backscatters. Forest shows intermediate backscattering, whereas calm water is a low backscatter because of its surface smoothness. The parameters that effect the backscattering coefficient are as follows:

- **Frequency**: The penetration depth of the radiation for target area and the relative surface roughness are dependent on the frequency of the incident electromagnetic energy.

- **Polarization**: Imaging radars can have different polarization configurations as discussed in section 2.1.1.3. The selection of polarization affect the penetration depth of radar wave. The information about the orientation and different layers of scattering elements on surface can be obtained from polarization chosen.

- **Roughness**: Roughness is independent of radar but it is a relative concept which depends on wavelength and incidence angle. According to the Rayleigh criterion, a surface is considered rough if

$$h > \frac{\lambda}{8cos(\theta_i)}, \tag{5}$$

and surface is considered smooth if

$$h < \frac{\lambda}{8cos(\theta_i)}, \tag{6}$$

where h is height of surface variation, λ is wavelength and θ_i is incidence angle.

- **Incidence Angle**: As discussed earlier, the incidence angle is the angle between the direction normal to the imaged surface and line of sight of incident wave. Backscattering coefficient σ^o varies with the angle of incidence for most natural targets.

- **Moisture**: The dielectric constant measures electrical properties of surface materials. Permittivity and conductivity are important features of dielectric constant. These two features are highly dependent on moisture content of the material under investigation. Moisture effect the dielectric properties of natural surface materials. Radar reflectivity increases with increase in moisture [13, 20].

2.1.3 Radar Image Geometry

The radar sensor mounted on the platform moves along the orbit in the direction of flight. The ground track of the orbit on the Earth's surface at nadir is shown in Fig.6. The microwave beam illuminates an area, or swath, on the earth's surface, with an offset from the nadir. The direction along-track is called azimuth and the direction perpendicular (across-track) is called range.

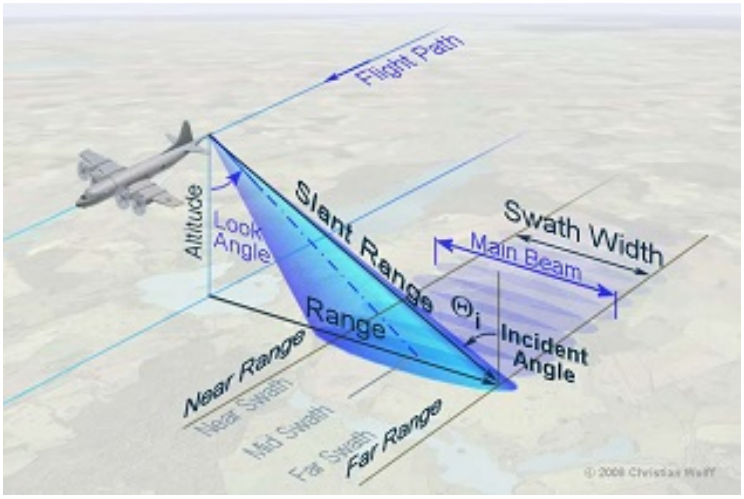

Figure 6: Side-looking viewing geometry of SAR (Image from [26]).

2.1.3.1 Viewing Geometry

In Fig.7, the viewing geometry of imaging radar sensors is shown. The part of the image that is closest to the nadir track is called near range and the portion of the image that is farthest from the nadir is called far range. The angle between the incident radar beam and local vertical is defined as incidence angle. Moving from near range to far range, the incidence angle increases. The difference between the incidence angle of sensor and local incidence depends on terrain slope and Earth curvature. Local incidence angle $\theta_{i,local}$ [12] is defined as the angle between the incident radar beam and the local surface normal as shown in Fig.7. The radar sensor measures the distance between antenna and object. This line is called slant range. The true horizontal distance along the ground corresponding to each measure point in slant range is called ground range [12].

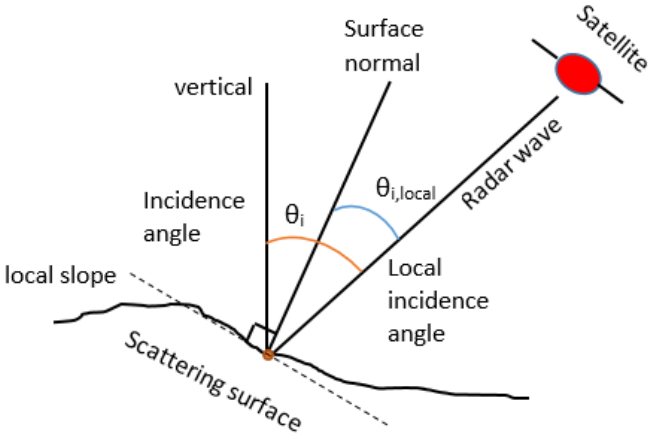

Figure 7: SAR incidence angle and local incidence angle.

2.1.3.2 Spatial Resolution

In imaging radars, spatial resolution is defined in two directions; azimuth and range directions. Resolution in the azimuth direction is called azimuth resolution and resolution in the range direction is called range resolution. The two parameters which define the spatial resolution in azimuth direction and slant range are: pulse length and antenna beam width. In case of Sentinel-1 SAR, the spatial resolution in IW mode is 2.7 x 22 m to 3.5 x 22 m [27].

2.1.3.3 SAR Range Resolution

Two dimensional (2-D) images are produced by SAR. One dimension in the image is called range (or cross track). Range resolution is determined by the width of the transmitted pulse. The narrow pulses produce fine range resolution. SAR range resolution can be categorized into slant range and ground range. In slant range, two ground objects are separated by a distance and received signal contains two different echoes. The distance between the ground objects define the spatial resolution in the slant range. Range has no effect on the resolution of slant range. However, incidence angle effects the resolution in ground geometry. Slant range resolution δr is constant along the range and is defined as

$$\delta r = \frac{c\tau}{2}. \tag{7}$$

Ground range resolution R_r is not constant across the range and is given as

$$R_r = \frac{c\tau}{2sin\theta}, \tag{8}$$

where c is the speed of light in vacuum, θ is look angle and τ is pulse length in [20].

2.1.3.4 SAR Azimuth Resolution

The second dimension in the image is perpendicular to range and is called azimuth (or along track). The spatial resolution in azimuth direction depends on the beam width and the range. The beam width of radar depends on wavelength and length of antenna. It is proportional to the wavelength and inversely proportional to the antenna aperture. This shows that large antenna will produce narrow beam and high resolution will be achieved in azimuth direction. SAR produces relatively fine azimuth resolution. This ability makes it different from other radars. Azimuth resolution is defined by the beam sharpness. The antenna length effects the sharpness of beam. If the antenna is large, it will focuses the transmitted and received energy into a sharp beam. Therefore, fine azimuth resolution will be achieved with sharp beam. The physical length of the radar R_a is proportional to azimuth resolution [20] and is expressed as

$$R_a = \frac{L}{2}, \tag{9}$$

where L is the length of the radar antenna. The spacecraft's height has no effect on azimuth resolution. Azimuth resolution increases with the decrease in antenna length.

2.1.4 SAR Image Types

A SAR image measures the radar backscattering contributions from the Earth's surface. This section discusses the differentiation between complex and detected SAR images as well as the concept of different SAR looks.

2.1.4.1 Complex Images

A complex SAR image $\overline{Z}$ can be expressed mathematically in its amplitude and phase form as

$$\overline{Z}(r,a) = A(r,a)e^{i\phi(r,a)}, \tag{10}$$

where r and a are image coordinates in range and azimuth, A is amplitude of the image and ϕ is phase of the image.

Complex SAR images are usually presented in slant range geometry and they have a single look. These kinds of complex images are called Single Look Complex (SLC) images. SLC image retain the amplitude and phase of the original SAR data [11].

2.1.4.2 Detected Images

As mentioned above, the SAR image contains both the amplitude and phase. The phase information from the SAR images is removed prior to be used for visualisation. Practically, this step is a part of processing chain and is called detection. The strength of the radar signal in each pixel is determined by the detection. Therefore, the resulting images are called the detected images. A square law detection is one of the detection processes. In square law detection, an intensity image $I = A^2$ is formed by multiplying the complex SAR image $\overline{Z}$ with its complex conjugate $\overline{Z}^*$ [11].

2.1.4.3 Single-look Image

SLC products are focused SAR images. They use orbit and attitude information from the satellite for geo-referencing [28], and are presented in slant-range geometry. The spatial resolution in SLC images is high. In single look images, the radar reflectivity and radiometric resolution becomes poor due to the speckle effect [11].

2.1.4.4 Multi-looked Image

Multi-looking is a process in which radiometric resolution of SAR data is improved at the expense of spatial resolution. In multi-looking operation, the synthetic aperture is divided into N parts and produce N lower resolution looks. These N looks are produced by single SAR data and then they are averaged together incoherently.

Another approach to multi-looking is to take an incoherent spatial average of a single look SAR image. Radiometric resolution is improved with both of these approaches as they are statistically and produce an N-look SAR image [11].

2.1.5 Distortions in Radar Images

The side-looking viewing geometry causes geometric and radiometric distortions in SAR imagery. Radar images experience variations in scale i.e., slant range to ground range conversion, foreshortening, layover and shadows [12].

2.1.5.1 Slant-Range Scale Distortions

Radar detect and measure ranges to ground objects in slant range. Therefore, the image has different scales moving from near to far range. This means that objects in near range are compressed with respect to objects at far range [12]. For proper interpretation, the image has to be corrected and transformed into ground range geometry. In Fig.8. the targets A1 and B1 are of the same size on the ground but their apparent dimensions appear different in slant range (A2 and B2). This causes targets to appear compressed in the near range as compared to the far range.

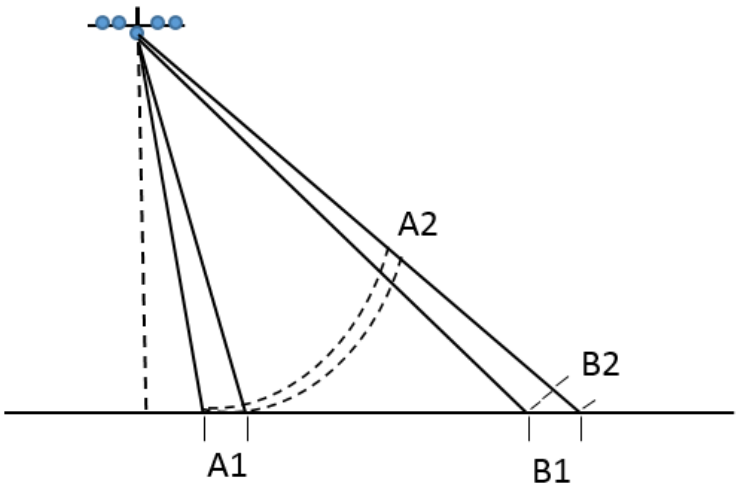

Figure 8: Slant-range scale distortion in SAR.

2.1.5.2 Terrain Induced Distortions

Terrain induced distortions are caused by relief displacement and it also effect radar imagery. Relief displacement is one dimensional and occurs in direction perpendicular to flight path. However, the displacement is reversed with targets being displaced towards the sensor. There are three effects that are typical for radar including foreshortening, layover and shadow shown in Fig.9.

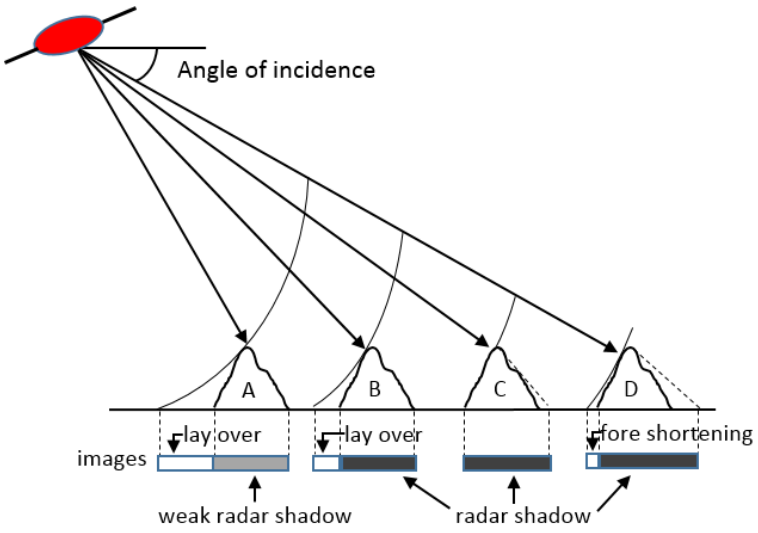

Figure 9: Geometric distortions in SAR images.

Foreshortening: Radar measures distance in slant range rather than true horizontal along the ground. The slope area is compressed in the image. The slope forms an angle in relation to the angle of the incident radar beam. The slope can be made shortened more or less on the basis of this angle. The distortion is at its maximum if the radar beam is almost perpendicular to the slope [12] as shown in feature D in Fig.9. Foreshortened areas appear bright in the radar image.

Layover: Layover occurs when the radar beam reaches the top of the slope earlier than the bottom [12] as shown in features A and B in Fig.9. At near range, the layover displacement is greater for smaller look angle. Layover areas also appear bright in the image and it can be considered as extreme case of foreshortening.

Shadow: Radar beam cannot illuminate the area of slope which is facing away from the sensor. Therefore, there is weak energy or no energy at all that can be backscattered to the sensor and those regions remain dark in the image. In Fig.9, the right side of feature A will be slightly illuminated as the slope is less steep than the look direction. The features C and D have slopes more steeper than look direction so the shadow extends beyond the slope area as shown in Fig.9. There will be no illumination when the slope facing away from satellite is parallel to the look direction as shown in feature B [12].

2.1.6 Radiometric Distortions

The above mentioned geometric distortions also have an influence on the received energy. Since the backscattered energy is collected in slant range, the received energy coming from a slope facing the sensor is stored in a reduced area in the image. This means it is compressed into fewer image pixels than should be the case if obtained in ground range geometry. This results in high digital numbers because the energy collected from different objects is combined. unfortunately this effect cannot be corrected. This is why especially layover and shadow areas in radar imagery cannot

be used for interpretation. However, they are useful in the sense that they contribute to a three dimensional look of the image and therefore help the understanding of the terrain structure and topography.

A typical property of the radar image is the so called speckle. It appears as grainy in the image shown in Fig.10. Speckle is caused by the interaction of the different microwaves backscattered from the object area. The wave interactions are called interference. Interference causes the return signals to be extinguished or amplified resulting in dark and bright pixels in the image even when the sensor observes a homogeneous area. Image interpretation is difficult as speckling degrades the quality of the radar imagery.

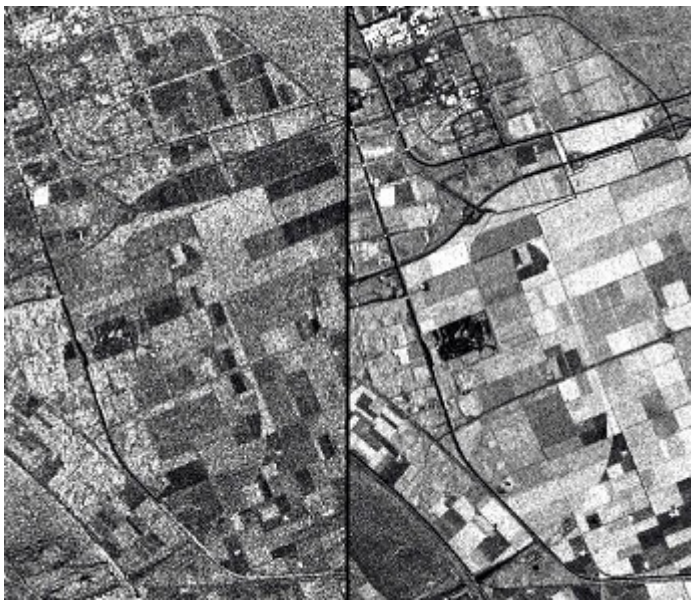

Figure 10: Radar speckle filtering (Image from [29]).

Multi-looking or spatial filtering can be used to reduce the speckle effect. In the case of multi-look processing, the radar beam is divided into several narrower beams. Each beam provides a look at the object. Using the average of these multiple looks, the final image is obtained. Multi-look processing reduces the spatial resolution [30].

Another way to reduce speckle is to apply spatial filters on the images. Speckle filters are designed to adapt to local image variations in order to smooth the values to reduce speckle. Speckle filtering enhance lines and edges to maintain the sharpness of the imagery.

2.1.7 SAR Processing

SAR processing is needed to reconstruct the imaged scene from a number of reflected pulses from each target on the surface of Earth. The reflected pulses are received by the antenna and registered in memory. The signal energy reflected from a point target is spread in two directions; range and azimuth. The Signal is spread in range by the duration of the transmitted pulse. In azimuth, the signal is spread by the duration it is illuminated by the antenna beam. SAR processing is carried out in two

dimensions and its purpose is to collect dispersed energy into a single pixel in the output image [31]. Range Doppler Algorithm (RDA) and Chirp Scaling Algorithm (CSA) are two methods of SAR processing. Here we will discuss RDA as it is most commonly used algorithm for processing SAR data.

2.1.7.1 Range Doppler Algorithm (RDA)

The range to the target changes as the point target passes through the azimuth antenna beam. The change in range causes variation in phase of the received signal as a function of azimuth. This phase variation over the synthetic aperture corresponds to the Doppler bandwidth of the azimuth signal. It allows the signal to be compressed in the azimuth direction. The variation in range to point target can cause variation in range delay which is larger than the range sample spacing. This is called range migration. This range migration of the signal energy must be corrected before azimuth compression can occur. The Range-Doppler algorithm is used to perform this correction [31].

There are various steps in RDA including range compression, azimuth Fast Fourier Transform (FFT), Range Cell Migration Correction (RCMC) and azimuth compression as shown in Fig.11.

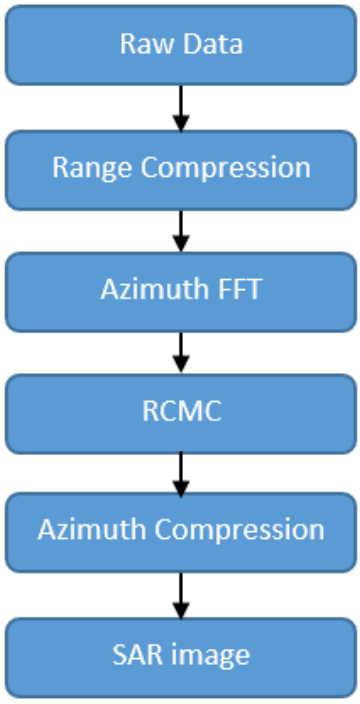

Figure 11: Steps for range doppler algorithm.

- **Range Compression**: Radar transmits linear FM pulses during SAR data acquisition. Linear FM pulse uses matched filter to give a narrow pulse. All the energy in the pulse is collected to the peak value. Applying match filtering

to received echo with its corresponding resolution and signal-to-noise ratio is called range resolution. Range compression is performed efficiently using FFT to each range line.Range compression data is obtained by applying an inverse FFT (IFFT) to each line. Range compressed data is then multiplied by a vector that correct the effects caused by the elevation beam pattern and range spreading loss on the amplitude [32].

- **Azimuth FFT**: Data is transformed into range doppler domain by using FFT in azimuth direction [32].
- **Range Cell Migration Correction (RCMC)**: RCMC is applied to correct the change in range delay to a point target. This range depends on the zero-Doppler range and on the angle from the satellite to the target. Ground targets with same zero-Doppler range have same range variation from the radar. The shape of the signal trajectories are same but they have azimuth displacement. Targets having the same zero-Doppler range can be expressed as a function of Doppler frequency. Due to this, RCMC performs efficiently in the range Doppler domain. The shift in range is needed to align the signal trajectory in a single range bin. It is determined independently for each azimuth frequency bin. The shift is then implemented by an interpolation in the range direction [32].
- **Azimuth Compression**: FFT is used to perform match filtering of azimuth signal. The match filtering of the azimuth signal is called azimuth compression. At this point, azimuth FFT has already been performed. The frequency response of the azimuth compression filter is precomputed using the orbital geometry. The azimuth filter also depends on range. Thus the data is divided into range invariance regions. The same basic matched filter is used over a range interval called the FM rate invariance region. The size of this invariance region must not be large enough to cause severe broadening in the compressed image. Focused SAR image is resulted after applying IFFT to each azimuth line [32].

2.2 InSAR Fundamentals

This section gives history and introduction to InSAR. Interferometric phase and coherence has been discussed to give the insight of InSAR basic theory and concepts for better understanding.

2.2.1 Introduction

SAR interferometry was first used for analyzing the surface of Venus and Moon from Earth by using the InSAR configurations with antennas [33]. The concept of topographic mapping by using synthetic aperture radar was first introduced by [34] and the first practical observations using airborne radar was presented in [35]. Goldstein et al. applied InSAR technique for the first time in space [36]. SEASAT-A

L-band SAR mission was used to generate DEM of the surface of Earth. With the launch of ERS-1 in 1991, JERS-1 in 1992, and RADARSAT in 1995, spaceborne InSAR study has increased dramatically. ERS-1 and ERS-2 tandem missions have improved the feasibility of InSAR in space [37]. They provide interferometric data with 24 hour temporal baseline. The Sentinel-1 constellation has also improved the potential of SAR interferometry in various applications including land cover mapping.

Over the past many years, digital elevatin models (DEM) of the Earth surface have been produced using Interferometric SAR technique [38]. Interferometry method uses two radar images to achieve coherence and phase difference between the images. The distance between the satellite and the ground object determines the phase of the SAR image. After coregistration, the phase of two images are combined to generate an interferogram. The phase of generated interferogram is high correlated to terrain topograpghy. Mostly DEMs derived from interferometry method use two antennas that are mounted on an aircraft or spaceborne platform, acquiring data simultaneously [38]. However, single sensor can be used for producing DEMs if same flight track is followed repeatedly. Temporal baselines effect interferometric coherence. Long temporal baseline decreases the coherence. The surface scatter changes its position and structure with time between radar acquisitions. This intorduces intrinsic changes in surface reflectivity causing phase noise to increase[39] and elevation measurement accuracy to decrase [40].

Remote sensing and geodesy uses interferometric SAR technique. This technique uses atleast two SAR images. Maps of surface deformation are generated by using the phase difference of the echoes received at the sensor after reflecting from ground surface. With InSAR, even centimetric scale changes in deformation can be detected and measured. It provide services for monitoring of natural hazards, for example, earthquakes, volcanoes and landslides. It also has applications in structural engineering, in particular monitoring of subsidence and structural stability.

2.2.1.1 Types of SAR Interferometry

There are two types of SAR interferometry; cross track interferometry (XTI) and along track interferometry (ATI). In corss track interferometry, two radar antennas are arranged across the track of the platform. XTI can be subdivided into single pass and repeat pass interferometry. Single pass XTI has two separate antennas mounted on the same platform. The SRTM mission uses single pass cross track interferometry. Repeat pass XTI uses single sensor mounted on the platform. It uses two separate passes of a single antenna as for Sentinel-1 mission. The repeat pass XTI always operates in the ping pong mode. However, the single pass arrangement can operate in either ping pong or standard mode depending on the design of the system [41].

Another type is along track interferometry. In ATI, radar antennas are arranged parallel to velocity vector of the platform. Similarly ATI, can be subdivided into single pass and repeat pass interferometry. Single pass ATI have two antennas arranged fore and aft on the fuselage of aircraft systems as shown in Fig.12. Their operating mode is either standard or ping pong. Repeat pass ATI has single radar antenna, following the same orbital track repeatedly. The along track interferometry

is important for detecting changes between SAR acquisitions. However, it is not sensitive to terrain variations since slant ranges are the same. Practically, in along track interferometry, the platforms do not follow the same path. Moreover, there is some along track separation as well as cross track separation which leads to detect terrain changes and topographic details [41].

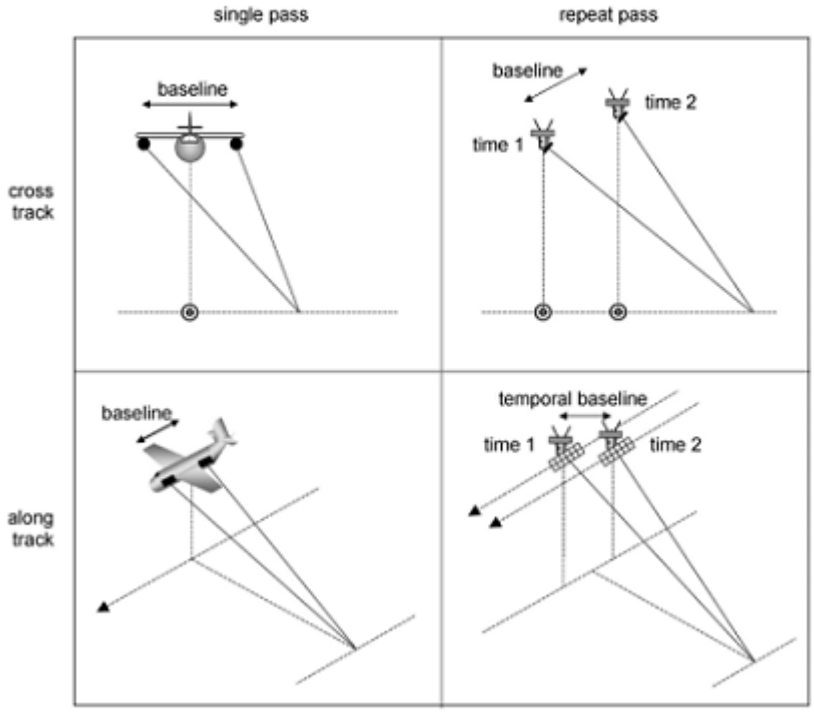

Figure 12: Types of SAR interferometry (Image from [42]).

Sentinel-1 mission orbits the Earth in the along track repeat pass configuration. The time interval between SAR acquisitions is 12 days with single satellite and 6 days with two satellites. The distance between the two satellites in the plane perpendicular to the orbit is called the interferometer baseline and its projection perpendicular to the slant range is the perpendicular baseline.

2.2.1.2 InSAR Baselines

SAR satellites are usually launched in Leo Earth Orbit (LEO) around the Earth at an altitude of about 500-800 km and revisit the same location on Earth after a specified time. The time period between the two successive SAR acquisitions is called ***temporal baseline***. The revisit time of satellites can be several days and extend to a month depending on the satellite orbit. Past studies have shown that the SAR observations with the shortest temporal baselines produce high coherence results. The temporal baseline for Sentinel-1 radar mission is 12 days with one satellite and reduces to six days with full constellation. However, the satellite location will be a bit changed while acquiring the next observation due to its restrictions in orbit control. In Fig.13, the ***perpendicular baseline*** defines the distance between two acquisition

spots perpendicular to the satellite viewing direction. For better interpretation of InSAR observations, baselines and wavelength are the main factors to be known.

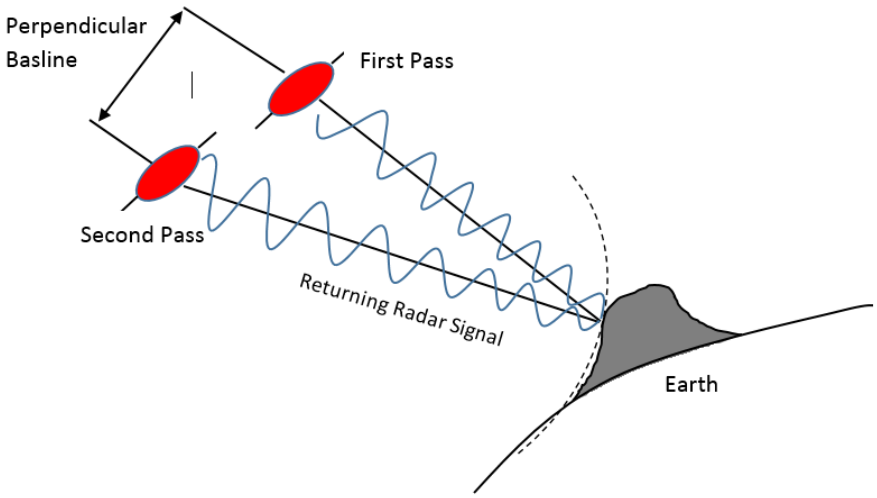

Figure 13: Perpendicular baseline for InSAR.

For InSAR, it is advisable to use suitable temporal and perpendicular baselines in combination with the area of interest and the availability of SAR data. In InSAR method, the phase from two or more images are compared in each pixel and phase is supposed to be consistent so that it can be used for comparison. If the images acquired have short temporal baseline, the scattering elements on the Earth surface will maintain its structure and position and high coherent values will be achieved otherwise there are chances that objects will change in case of longer temporal baseline. Changes affect coherence and can lead to decorrelation between the two pixels. ERS 1/2 mission has 24 hours temporal baseline between the acquisitions and therefore provides high coherence results. This causes a loss of coherence and eventually leads to complete decorrelation between the two pixels. Perpendicular baseline also has an effect on coherence. Larger baselines causes loss in coherence as target looks different with viewing angle.

2.2.2 Interferometric Phase for Terrain Altitude Measurement

In repeat pass interferometry, SAR systems observe the point scatterers on the surface of Earth from two slightly different look angles. The two observations in ground resolution cell cannot be taken from exactly the same location due to some orbit control limitations. The interferometric phase of the SAR image pixels is the difference in the travel paths of the two SAR sensors to the considered ground resolution cell. This difference cancels out any phase contributed to the interferometric phase by the point scatterers. In passing from identified reference cell to another, introduces variation in the travel path difference Δr [43]. The travel path variation depends on geometric parameters and can be expressed as

$$\Delta r = -2\frac{B_n q_s}{R}, \tag{11}$$

where B_n is the perpendicular baseline, R is the range between sensor and target, and q_s is the displacement between the resolution cells along the perpendicular to the slant range. The Δr expression is an approximation for small baselines and small distance resolution cells. The interferometric phase variation $\Delta\phi$ [43] is proportional to Δr divided by the transmitted wavelength λ and can be expressed as

$$\Delta\phi = \frac{2\pi\Delta r}{\lambda} = \frac{4\pi}{\lambda}\frac{B_n q_s}{R}. \tag{12}$$

2.2.2.1 Interferogram Flattening

The interferogram flattening is a part of InSAR processing and provides accurate topographic information. The purpose is to remove the phase contribution from flat earth as it has nothing to do with surface deformation or topographic elevation [44]. The interferometric phase variation $\Delta\phi$ can be divided into two terms. In equation 13, the first term represents a phase variation proportional to the altitude difference between the point targets. The second term represents a phase variation proportional to the slant range displacement of the point targets [43].

$$\Delta\phi = -\frac{4\pi}{\lambda}\frac{B_n q}{Rsin\theta} - \frac{4\pi}{\lambda}\frac{B_n s}{Rtan\theta}, \tag{13}$$

where θ is the radiation incidence angle with respect to the reference, q is the difference in altitude between targets, and s is the displacement of the targets in slant-range. The calculation of perpendicular baseline requires precise orbital data. For interferogram flattening, the second phase term is calculated and subtracted from the interferometric phase. As a result, it generates a phase map proportional to the relative terrain altitude [43].

2.2.2.2 Height of Ambiguity

The height of ambiguity h_a is the amount of height change that generates 2π change in interferometric phase. The h_a leads to an interferometric phase change of 2π after interferogram flattening. The height of ambiguity is inversely proportional to the perpendicular baseline [43] and is expressed as

$$h_a = \frac{\lambda Rsin\theta}{2B_n}. \tag{14}$$

Practically, the phase noise is equivalent to smaller altitude noise so longer baselines gives accurate altitude measurement. Moreover, the higher the baseline, the smaller the topographic height needed to produce a fringe of phase change or, the longer the baseline is the stronger the topographic imprint. The perpendicular baseline needs to be in the limit, otherwise interferometric signals decorrelate and no fringe will be generated. To sum up, signal to noise power ratio is maximised by optimum perpendicular baseline [43].

2.2.3 Interferometric Coherence

There are various sources of noise which effect the quality of interferometric phase including system noise, terrain change, images misregistration, geometric decorrelation etc [45]. System noise and terrain change cannot be avoided. On the other hand, images misregistration and geometric decorrelation can be taken care of. System noise is small comparatively with sensed signals, and the processing noise can be controlled if the processor is designed to preserve the phase [46]. It is observed that fringe quality is mainly degraded with scattering change in time and volumetric effects. The complex interferometric coherence γ is the complex correlation coefficient between two SAR images [11] and is expressed as

$$\gamma = \frac{E[\bar{Z}_1 \bar{Z}_2^{\star}]}{\sqrt{E[\bar{Z}_1]^2 E[\bar{Z}_2]^2}}, \tag{15}$$

where $E[]$ denotes the expected value and * denotes the complex conjugate. The phase of the complex coherence gives the expected value of the interferometric phase of the observed pixel. The interferometric phase is the phase of the complex correlation coefficient [11] and is expressed as

$$\phi = arg\{\gamma\} = arg\{E[\bar{Z}_1 \bar{Z}_2^{\star}]\}, \tag{16}$$

and its two dimensional map is called the interferogram.

The interferometric coherence carries key information about the target depending on the radar wavelength chosen. The coherence varies from 0 to 1 due to scaling by the denominator. Incoherence is indicated with 0 and perfect coherence is indicated with 1. The presence of noise in interferometric phase causes decrease in coherence. High coherence values are achieved when both images experience same or nearly the same interaction with ground scatterers. This way both images will have a similar speckle pattern [47]. The signal to noise ratio (SNR) of the interferogram can be expressed in relation to coherence [11] as

$$SNR = \frac{|\bar{\gamma}|}{1 - |\bar{\gamma}|}. \tag{17}$$

2.3 Land Cover Classification

Land cover is a physical representation of various processes taking place on the Earth's surface. It provides information about the various contents by which the land is occupied including natural sources such as forest and woodlands. It also indicate the way in which the land is being used. Classification is a way of classifying land cover contents into different classes using well defined classifiers. It is defined as the ordering or arrangement of objects into groups or sets on the basis of their relationships [48]. A classification is a system of recognizing and assigning class names to different objects and using a criteria to distinguish relationship between these classes. Classification needs an objective criteria which needs to define class boundary depending on precision, clarity and quantity. A classification procedure

should be independent of any scale and source. Classes can be applied to any level of details and sources of collecting information must not be restricted means it can be a satellite imagery, aerial images, on field data or using fusion of sources.

The major goal of satellite remote sensing is acquiring land images, interpretation and classification of features. Besides photo interpretation, quantitative analysis is a form of classification which labels every pixel in an image to particular spectral class. The purpose of image classification is assigning classes to all image pixels. Every pixel has a digital number (DN) which defines the spectral reflectance and is a basis of classification. Classification can be divided in to two basic methods: supervised classification and unsupervised classification. The supervised classification is the essential tool used for extracting quantitative information from remotely sensed image data [49]. Using supervised method, training samples are collected from the available image pixels for each class of interest. This operation is called training. Classifiers are trained using the selected training samples to assign labels to every pixel in the image. Another method of classification is unsupervised classification. Unsupervised classification does not require any prior knowledge of the classes to label the pixels. It uses clustering algorithms to assign classes to image pixels [49].

2.3.1 Classification Techniques

Many classification methods have been developed and used for generating land cover maps [50]. Supervised and unsupervised classification are the two basic classification techniques. Here, we will give the overview of both classification methods.

2.3.1.1 Unsupervised Classification

The unsupervised classification does not use prior knowledge of training samples to assign classes to the image data. In this method, same values are assigned to the pixels belonging to same class. Clustering algorithm uses natural groupings or clusters. The number of clusters and band selection is done by the user. Image classification tools generate groups or clusters using this information. Different algorithms are used for image clustering, for example, ISODATA and K-means. Reference data is used to compare with the results to decide the classes of clusters or groups.

Image pixels are grouped together based on their reflectance or emittance properties. These groupings are called *clusters*. In unsupervised classification, the operator manually distinguishes each cluster with respect to land cover class. There are high chances that single land cover class is represented by multiple clusters. It is then advisable to merge the clusters into one land cover type. The unsupervised image classification technique is commonly used when no sample sites exist. The unsupervised classification has three main steps: generation of clusters, assigning classes and validation of results [12]. In Fig.14, the flow diagram of unsupervised classification is shown.

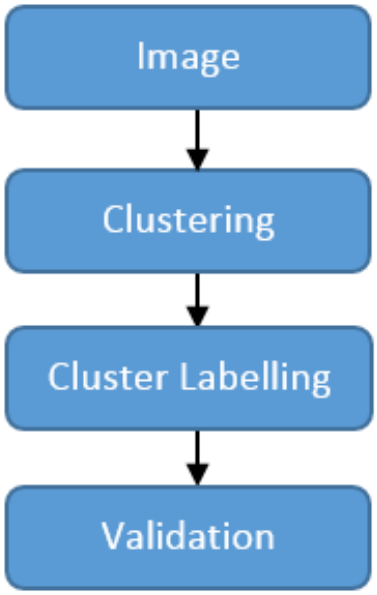

Figure 14: Unsupervised classification flow diagram.

2.3.1.2 Supervised Classification

The supervised classification uses prior knowledge of training samples to train the classifiers and to assign classes to the image data. This procedure of pixel categorization is called the supervised. Supervised classification uses reference data for extracting spectral features of some areas from knonw land cover types [51]. The extracted areas are called "training areas". Training samples generate spectral signatures. These signatures are then used to train the classifier for classifying the spectral data into a thematic map [52]. Image pixels are then classified depending on the similarity of spectral features with the spectral features of the training areas. The analyst identifies the training area and develops a numerical description of the spectral attributes of the class or land cover type. During the training stage, size, shape, location and orientation of pixels for each class is determined. The spectral signatures are compared with the unknown pixels in the image. The unknown pixels will be labelled according to their digital resemblance with the nearby class. Similarly, supervised classification has three main steps: selection of training areas, pixel labelling and validation of results [12]. The flow diagram of supervised classification is shown in Fig.15.

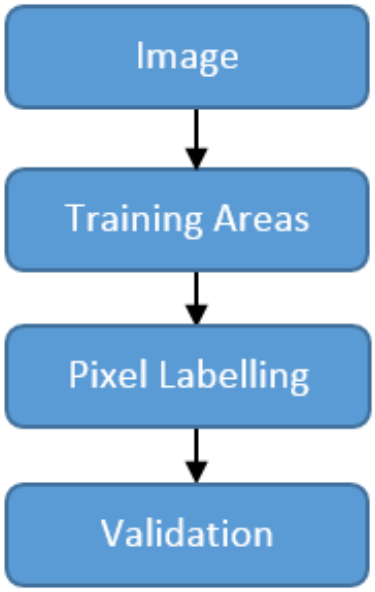

Figure 15: Supervised classification flow diagram.

2.3.2 Types of Classifier

In this study, supervised classification technique has been used for land cover classification. Supervised classification has different classifiers to be used, depending on their purpose and performance. Euclidean distance and k-nearest neighbour (kNN) classifiers are utilised for the study purpose and will be discussed further.

2.3.2.1 Euclidean Distance

Euclidean distance has nothing to do with machine learning specifically. It is only one of the many available options to measure the distance between two data objects. However, many classification algorithms (for e.g. K-Nearest Neighbour, Minimum Distance Classifier etc) use it to either train the classifier or decide the class membership of a test observation and clustering algorithms (e.g. k-means) use it to assign membership to data objects among different clusters.

Euclidean distance D measures the distance between two points in any number of dimensions. It is expressed mathematically as the square root of the sum of the squares of the differences between the respective coordinates in each of the dimensions [53]

$$D(m,p) = \sqrt{\sum_{i=1}^{n}(m_i - p_i)^2}, \tag{18}$$

where m is the unknown feature vector, p is the training sample and n shows the number of dimensions of feature vectors.

2.3.2.2 k-Nearest Neighbour (kNN)

Over the past many years, various classification algorithms have been developed and utilised for classifying land cover types. The kNN algorithm is robust, simple to understand and it works efficiently. It is used as benchmark for other classifiers such as Neural Networks (NN) and Support Vector Machines (SVM).The kNN is a non-parametric classifier used for classifying a point based on closest neighbour in the feature space. It is considered simplest algorithm as compared to other techniques. The validated reference data is used for selecting the training samples. The class labels and feature vectors are stored in the training step. The kNN algorithm assign labels according to k-nearest neighbours of the unlabelled point using the distance metric. In this study, Euclidean distance metric is used. The Classification steps using kNN algorithm can be shown in the flow diagram in Fig.16.

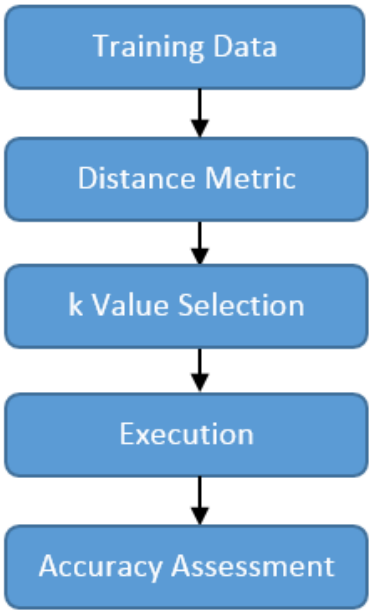

Figure 16: kNN algorithm flow diagram.

The working principle of kNN algorithm is to form a majority vote between the k most similar instances to unlabelled query point. Similarity is determined based on the distance metric between two data points. A popular choice is the Euclidean distance given in the equation.18. The kNN classifier runs through the whole dataset computing similarity between the unlabelled point and each training point. The value of k is selected odd in order to avoid the tie situations. In Fig.17, the unknown observation belongs to class-2 if the value of k is 3, otherwise if the value of k is 5 then it belongs to class-1.

Although kNN is the simplest of all machine learning algorithms but its computation is expansive [53]. The computation time increases since the distance metric measures the distance between every training sample and unknown feature. The effectiveness of the algorithm decreases with the increase in the number of feature dimensions.

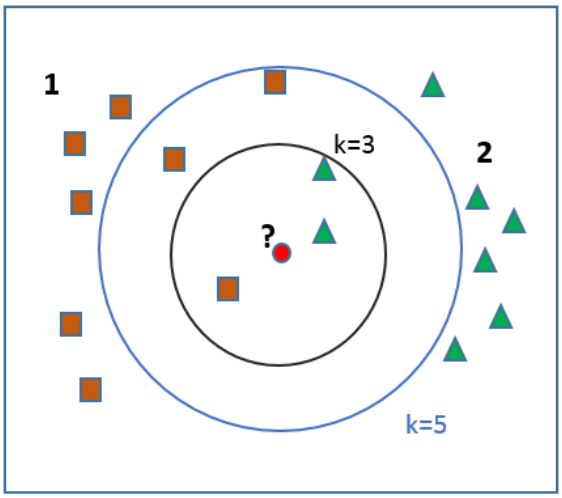

Figure 17: Illustration of kNN algorithm.

2.3.3 Training Data Characteristics

Training phase is a critical step in supervised classification. Training samples are collected from relatively uniform areas on the ground. The selection of trainig samples are done in a way to avoid mixed pixels. Mixed pixels are a major problem in land cover classification and contain two or more classes which lead to errors in classification. However, the collection of training data is generally a critical issue and, therefore, the size of the training data should be kept small [54]. For correct characterization of the classes, the training data should be large enough.

The classification process has two important parts which include the collection of training areas and data testing. The training data is used to train the classifier, which then classify the unknown pixels depending on their similarity between labelled and unlabelled provided points. The validation of classification results is done with test data i.e. comparing known classification with the classified results obtained by applying the developed methodology. To achieve better accuracy, it is advisable to utilise complete and validated training data. Well defined statistics should be used to separate the classes. Representative distributions can be found by proper selection of size and spatial distribution of training sites [55].

2.3.4 Reference Data Characteristics and Accuracy Assessment

In image classification, validation of classified results is done by accuracy assessment. Accuracy assessment is a way to analyze the errors which are introduced during the classification process due to some reasons. The sample testing data is acquired from the reference data for the assessment of the classification accuracy. The testing data is supposed to be independent of the training samples. In many studies, the same data sets have been used for training and testing, resulting in an optimistic bias in classification accuracy [56]. Errors in the reference data is also an important issue as they are obtained from different sources with varying accuracies including existing maps, aerial photographs, GPS surveys or a fusion of data. The maps

may have errors relating to update and compilation. The aerial photographs may have positional inaccuracies due to titlt and relief displacement. GPS surveys are expansive and introduce other errors. Hence, data is not error free irrespective of their source. Any error in the reference data may result into a conservative bias in the classification accuracy [57].

Confusion matrix is an accuracy measure. It is used as a quantitative method to characterize image classification accuracy [58]. It has the information about actual and predicted classifications done with the classification methodology. The actual classifications can be shown in rows and predicted in columns or vice versa. The diagonal elements shows the correctly identified pixels. The total accuracy is calculated by dividing the sum of the pixels in diagonal entries with the total number of pixels. The non-diagonal entries represent classification errors. Pixels belonging to one class, when assigned to another class introduces classification errors. There are two types of classification errors: omission errors and commission errors. Omission error occurs when pixels are left out of the class being evaluated. On the other hand, errors of commission occur when pixels are included in the wrong class being evaluated. User accuracy is the number of the correctly identified pixels of a class, divided by the total number of pixels of the class in the classified image. Producer accuracy is the number of correctly identified pixels divided by the total number of pixels in the reference image [58].

3 Study Material

This chapter includes the test site and overview of Sentinel-1 and Sentienl-2 missions. Single pair Sentinel-1 dataset and one Sentinel-2A optical image is listed. Corine land cover model used for this study is also discussed.

3.1 Area of Interest

The area of interest is located in south of Estonia. The test site (54.18 km x 35 km) is situated in Soomaa National Park in south west of Estonia (58° 24'N, 25° E) [59] as shown in Fig.18. The area is covered with major portion of floodplain grasslands, raised bogs, open fields and paludified forests. Lakes and a portion of Pärnu River is present in our research area. The study area is surrounded by large mires and rivers of the Pärnu River basin (Halliste, Raudna and Lemmjõgi) [59]. The Soomaa site is elevated 20-30 m above sea level.

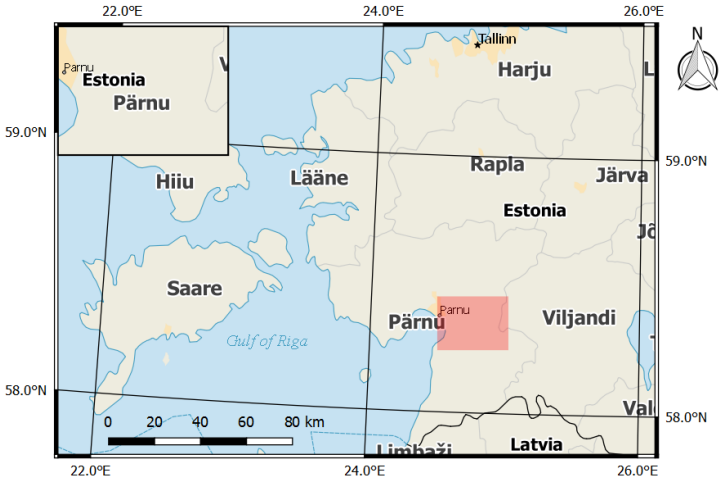

Figure 18: Study area location map.

3.2 Sentinel-1 Satellite Mission

The Sentinel-1 mission is based on a constellation of identical synthetic aperture radar satellites shown in Fig.19. The constellation is currently comprised of A and B units. Sentinel-1 constellation provide data continuity to European Space Agency's previous SAR missions including European Remote Sensing (ERS) and ENVISAT [60].

Sentinel-1 satellites are operating in C-Band (freq: 5.405 GHz). They provide continuous radar imagery in all weather conditions. They can operate during day and night. The sentinel-1 constellation provides 24/7 global coverage with reliable data. With the launch of Sentinel-1B, the revisit time has improved to 6 days with two satellites. Sentinel-1 disseminate high speed data to support various applications, for example, marine monitoring, land monitoring and emergency services.

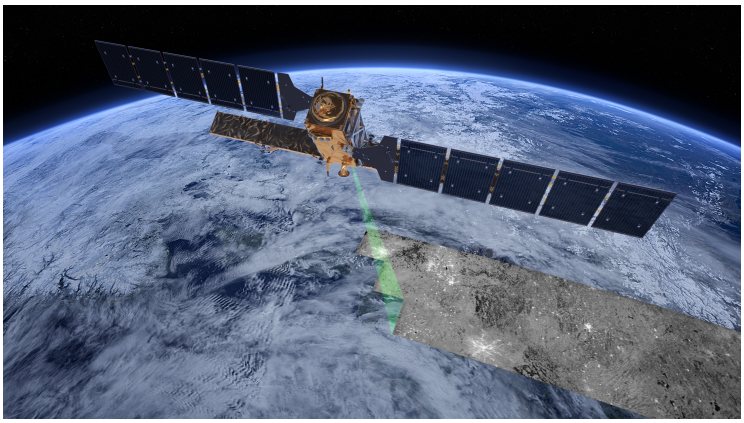

Figure 19: Sentinel-1 remote sensing satellite (Image from [61]).

The sentinel-1 constellation orbit is a Sun-synchronous and near polar. The circular orbit is 693 km high above the surface of Earth. It has an inclination of 98.18 deg. It has 12 days repeat cycle with one satellite and 6 days with two satellites. The operational life span of Sentinel-1 is 7 years. The Sentinel-1 carries C-band SAR sensor which provide imagery in medium and high resolution. The Sentinel-1 can potentially provide night imagery to land monitoring, marine monitoring, oil spill mapping and climate change monitoring. It provides conflict free operations as operational modes for land and sea monitoring are separate. The Interferometric wide (IW) is the main operational mode over land. It has 250 km wide swath with high geometric and radiometric resolutions. The incidence angle range in IW mode for Sentinel-1 mission is 29.1°-46.0° [62]. The sentinel-1 SAR instrument acquire data in four exclusive modes but we will discuss Interferometric Wide (IW) swath mode in more detail.

3.3 Interferometric Wide Swath Product

Sentinel-1 satellite acquires data using four modes shown in Fig.20. These four modes are:

- Stripmap (SM)- Antenna operates in a fixed direction in strip map mode. It uses 5 m by 5 m spatial resolution and 80 km of swath for acquiring data [63].
- Interferometric Wide Swath (IW)- This mode has 5 m by 20 m spatial resolution and wide swath width of 250 km for coverage. Interferometric wide is the primary mode over land for Sentinel-1 [63].
- Extra Wide Swath (EW)- EW mode has five sub-swaths as compared to IW mode and provides a low resolution of 20 m by 40 m [63]. It is basically used for services like maritime where wide coverage is required.
- Wave (WV)- In this mode, data acquisition is done with 5 m by 5 m spatial resolution and stripmap imagettes of 20 km by 20 km. These imagettes are acquired every 100 km, alternately on two different incidence angles [63].

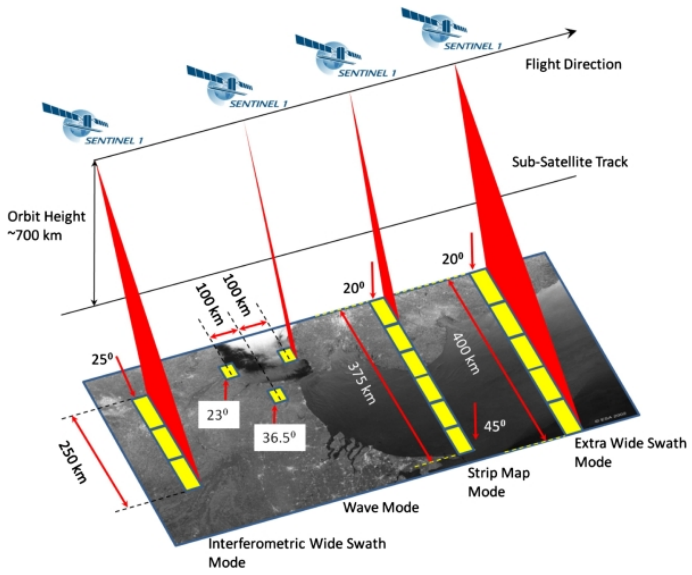

Figure 20: Sentinel-1 data acquiring modes (Image from [63]).

The Sentinel-1 interferometric wide (IW) swath mode uses Terrain Observation with Progressive Scanning SAR (TOPSAR) imaging technique to acquire data. Interferometric wide (IW) mode has three swaths. TOPSAR working principle is same as ScanSAR in range direction. However, antenna beam can be electronically switched to and fro in the azimuth direction [62] shown in Fig.21. TOPSAR technique acquires data in bursts. Antenna beam is switched between adjacent sub-swaths during data acquisition. Going from one pass to another, bursts need to be synchronised to obtain aligned interferometric pairs. As mentioned above, the IW mode acquires data with a wide swath of 250 km at 5 m by 20 m spatial resolution in range and azimuth respectively [63]. The IW mode is the primary operational mode over land for Sentinel-1. The SLC products used in this study are in interferometric wide swath mode.

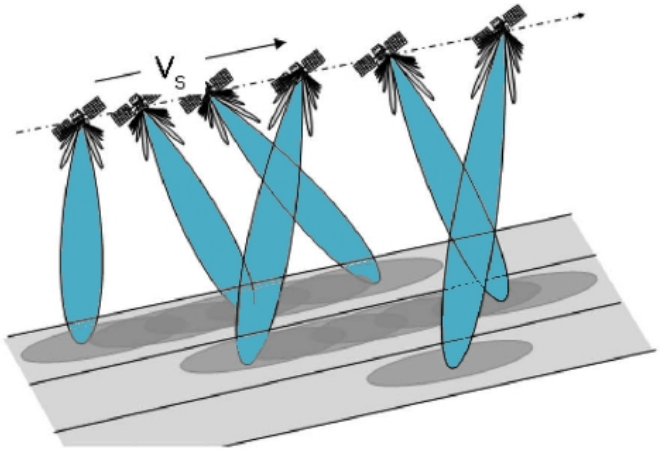

Figure 21: Sentinel-1 interferometric wide swath (Image from [62]).

In IW SLC product, each sub-swath consists of a series of bursts. Each burst is then processed as a separate SLC image. Single SLC product in IW mode has three images in single polarization and six with dual polarization as it contains one image per sub-swath. The black-fill demarcation zone is present between images per sub-swath [64]. This demarcation zone is removed during the processing chain by using de-bursting operation. Sentinel-1 IW mode has some characteristics listed in Table 1.

Parameter	**Value**
Swath width	250 km
Incidence angle range	29.1°-46.0°
Sub-swaths	3
Azimuth steering angle	±0.6°
Azimuth and range looks	Single
Polarization	Single (HH,VV), Dual (HH+HV, VV+VH)

Table 1: Characteristics of Sentinel-1 interferometric wide swath mode.

3.4 Sentinel-1 Dataset

Single pair of level-1 SLC dataset from both Sentinel-1A and Sentinel-1B has been used in our study. SLC products are geo-referenced and provided in slant-range geometry. Sentinel-1 SLC data products provided by ESA comprises of complex radar imagery with amplitude and phase are listed below.

1. S1A-IW-SLC-1SDV-20160930T043407-20160930T043434-013277-015262-995E
2. S1B-IW-SLC-1SDV-20161006T043322-20161006T043349-002381-004063-E216

Sentinel-1A and Sentinel-1B SLC data product parameters used here are listed in Table 2.

Parameter	**File 1**	**File 2**
Satellite	S1A	S1B
Type	SLC	SLC
Acquisition	30Sept16	06Oct16
Track	80	80
Orbit	13277	2381

Table 2: Sentinel-1 SLC data product parameters.

The pair selected for this study is of autumn season. The winter images for Sentinel-1B were not available due to sea-ice monitoring priority over Baltic. Due to unavailability of six day winter images, the product parameters can not be calculated and compared. The selected image pair has the most suitable perpendicular baseline and heigh of ambiguity with six days gap.

3.5 Sentinel-2 Satellite Mission

Sentinel-2 mission is a constellation of Sentinel-2A and Sentinel-2B satellites shown in Fig.22. It is a part of Copernicus programme developed by European Space Agency (ESA). Sentinel-2 mission is designed specifically to perform Earth observations. The mission provides high resolution optical imagery with data continuity for currently operational SPOT and Landsat missions [65].

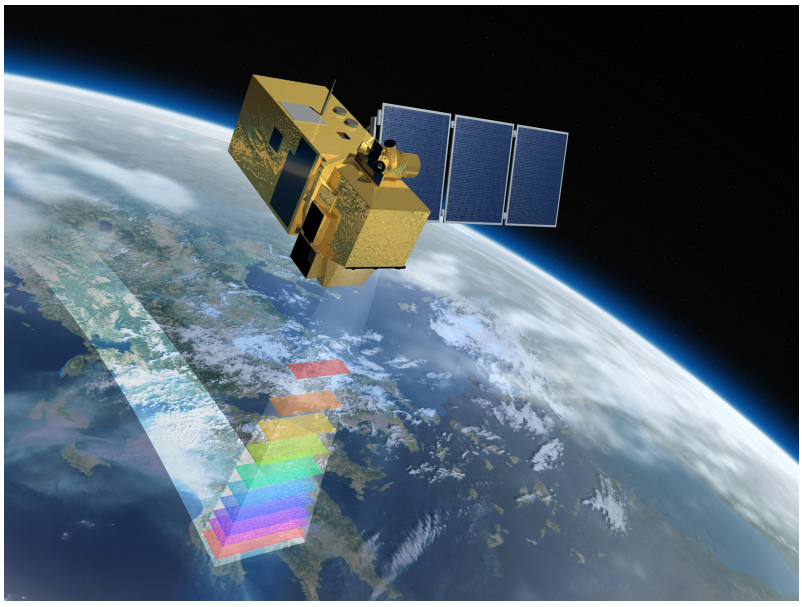

Figure 22: Sentinel-2 remote sensing satellite(Image from [66]).

The Sentinel-2 is a land monitoring constellation that perform terrestrial observations. It provide services to monitor forestry, marine environmental monitoring, detecting changes in land cover and managing natural disaster. The revisit time is of 10 days for one satellite and 5 days with 2 satellites. Sentinel-2 has 13 spectral bands which provides global coverage with high resolution multispectral imagery [65].

In this study, a single optical image of Sentinel-2A satellite has been employed as a reference image for exact feature extraction for classification purposes in QGIS, which will be explained in more detail in coming chapters. Sentinel-2 data is available free on ESA data hub of sentinels for scientific purposes. Sentinel-2A optical image used in the study was acquired on 24^{th} August, 2015.

- S2A-OPER-PRD-MSIL1C-PDMC-20161003T101059-R036-V20150824T094006-20150824T094301

Sentinel-2A optical image (109 km x 109 km) is downloaded from Sentinels data hub with 0.0 percentage cloud coverage. Natural colour RGB image has been generated in SNAP using B2, B3 and B4 bands as shown in Fig.23.

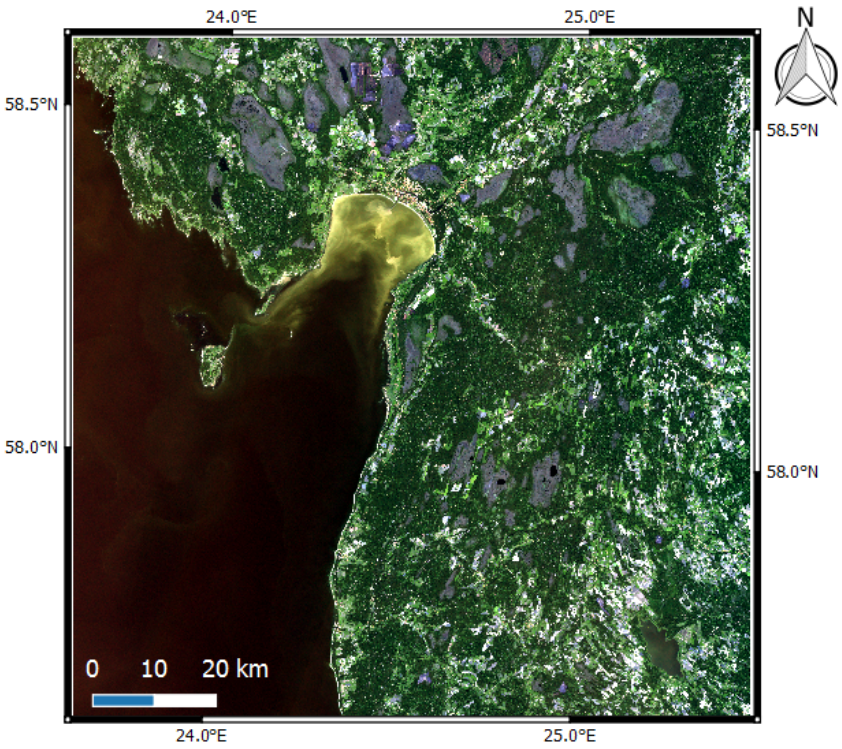

Figure 23: Sentinel-2A optical image

The parameters for Sentinel-2A optical image are listed in Table 3.

Parameter	**File 1**
Satellite name	Sentinel-2
Satellite number	A
Product Type	S2MSI1C
Cloud cover percentage	0.0
Acquisition	24Aug2015
Orbit number	891
Pass direction	Descending
Relative orbit	36

Table 3: Sentinel-2A data product parameters.

3.6 Corine2012 Land Cover Model

European Union initialised a Corine programme in 1985. Corine stands for *coordination of information on the environment*. The database contains geographic land cover/land use information for most of the European countries and it has been under the control of European Environment Agency (EEA). The land cover inventory consisting of 44 classes is presented as cartographic product, at a scale of 1:100 000 [67]. Spot and Landsat missions are the bases for corine mapping and its database is available for most of the European countries.

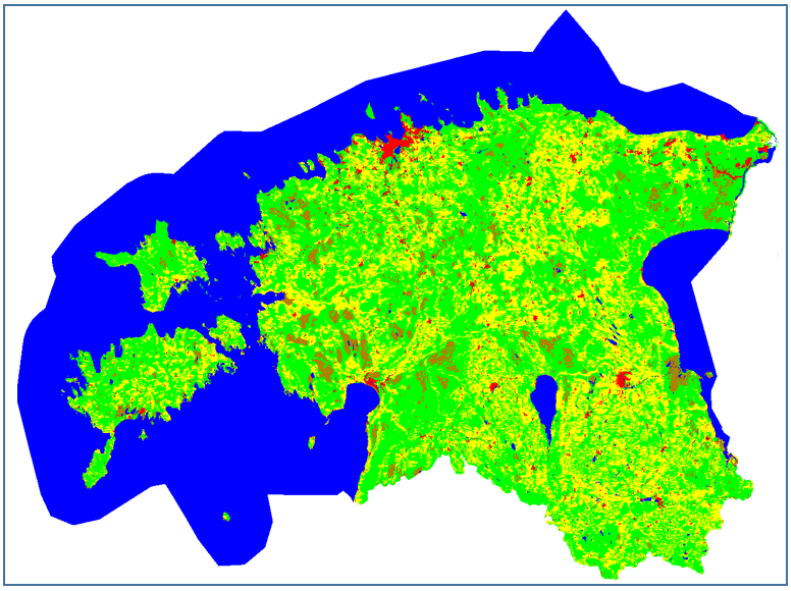

Figure 24: Corine2012 model for Estonia.

Since 1985, three land cover layers have already been produced in the years 2000, 2006 and 2012. Corine map has 44 classes which are categorized into three levels. The first level is comprising of five major classes listed as:

- *Artificial*
- *Agricultural*
- *Forest and semi-natural areas*
- *Wetlands*
- *Water bodies*

The second level has 15 classes. It contains detailed information about physical entities of urban area, forestry, water, etc [67]. Finally, 44 classes are present in level 3. The CLC2012 model was acquired for our study over the area of Estonia shown in Fig.24. Area of interest was selected from Corine2012 map and features are extracted by overlaying with the Sentinel-2 optical image for training samples.

4 Research Methodology

In this chapter, processing chains for interferogram formation and backscattering have been set up and applied to Sentinel-1 dataset. Feature extraction for training samples, land cover classification techniques and methods are presented. The software tools used in the study are Matlab, Sentinel-1 toolbox and QGIS.

4.1 Interferometric Coherence Processing Chain

In this section, the set-up of interferometric coherence processing chain and its implementation on Sentinel-1 SAR images is discussed. Two Sentinel-1 SAR acquisitions are used with a six days temporal baseline. One SLC image was acquired on 30^{th} of September, 2016 from Sentinel-1A and other was acquired on 06^{th} of October, 2016 from Sentinel-1B. Our test area is located in the IW3 sub-swath as shown in Fig.25.

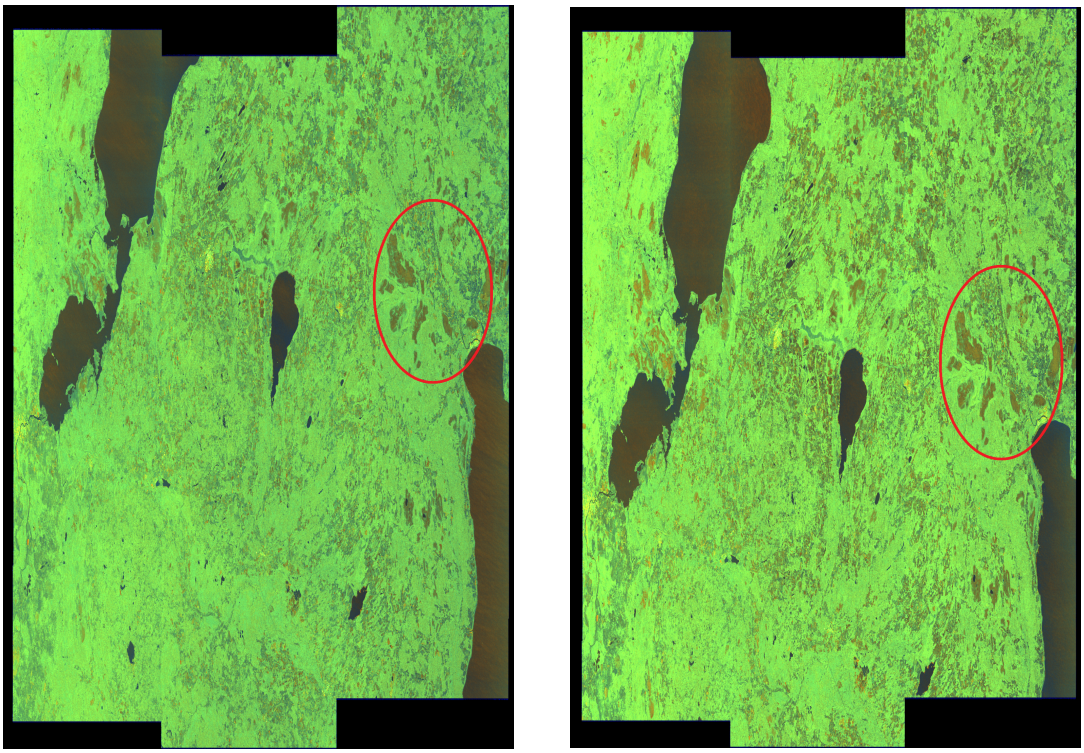

(a) 30^{th} Sept, 2016. **(b)** 06^{th} Oct, 2016.

Figure 25: 30^{th} Sept, 2016 from Sentinel-1A and 06^{th} Oct, 2016 from Sentinel-1B.

Interferometric coherence processing requires at least two or more SAR images for co-registration. It is advisable to perform TOPSAR splitting operation before co-registration. Splitting helps to select the desired number of bursts and IW sub-swaths over the area of interest and polarization can also be selected. Selection of correct sub-swath and number of bursts helps in processing and takes less time. Orbit file is automatically downloaded by the SNAP. Orbit file contains information about the position and flying direction of the Sentinel-1. Orbit information is applied

to the selected SLC products. In co-registration both the master and slave images have ground targets contribution to the same pixel. Slave image pixels are aligned with the master pixels to get high accuracy. Multiplying of master image with the complex conjugate of slave image produces interferogram. The complex SAR image contains both the amplitude and phase information. The amplitude of both the images is multiplied while the phase represents the phase difference between the two images. The interferometric phase depends only on the difference in the travel paths from each of the two SARs to the considered resolution cell. The Demarcation zones between the bursts are then removed by applying TOPS de-bursting operator shown in Fig.26. In interferometric coherence processing chain, only three bursts (4-6) from IW3 swath in VV polarization are used.

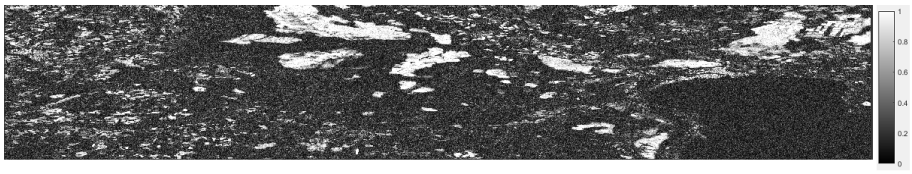

Figure 26: De-bursted interferometric coherence of image pair 30^{th} Sept-06^{th} Oct, 2016 in VV polarization. The coherence scales from 0 to 1. Dark areas are indicating low coherence and bright areas indicating high coherence.

Flattening of interferogram is done by using topographic phase removal. The operator simulates an interferogram based on the referenced DEM and subtract it from processed interferogram. Some factors like temporal decorrelation, geometric correlation or processing error introduces noise in the interferometric phase. This noise is removed by applying phase filtering.

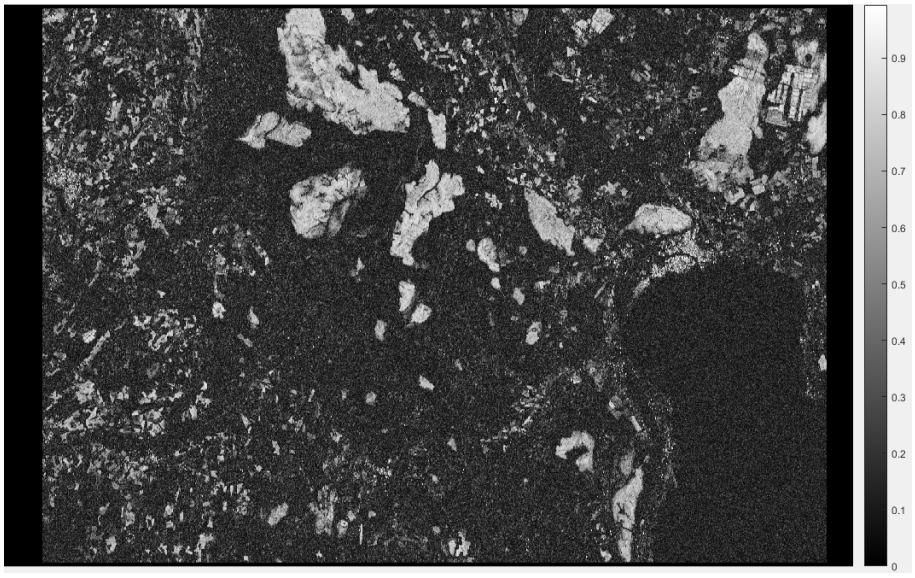

Figure 27: Multi-looked interferometric coherence of image pair 30^{th} Sept-06^{th} Oct, 2016 in VV polarization. The coherence scales from 0 to 1. Dark areas are indicating low coherence and bright areas indicating high coherence.

Multi-looking is applied with 4 by 1 at range and azimuth respectively as shown in Fig.27. Multi-looking is a procedure used to damp the effect of speckle. Multi-looking reduces the standard deviation of the noise level and introduces Gaussian distribution of noise in the SAR image at the cost of decreased resolution. Multi-looking improves radiometric resolution but spatial resolution is degraded by averaging over range and azimuth.

Terrain topography affects both the position of the given point on Earth and the brightness of the radar reflection. Corresponding position of each image pixel on Earth is acquired by reconstructing the imaging geometry using SAR geocoding. Geometric distortions are cuased by the side looking geometry of the SAR images and there is no one-to-one relationship exist between radar and map geometries [68]. Therefore, a DEM is used to accurately perform geocoding and terrain correction shown in Fig.28. The geometric terrain correction removes the effect of side looking geometry of the SAR acquisitions.

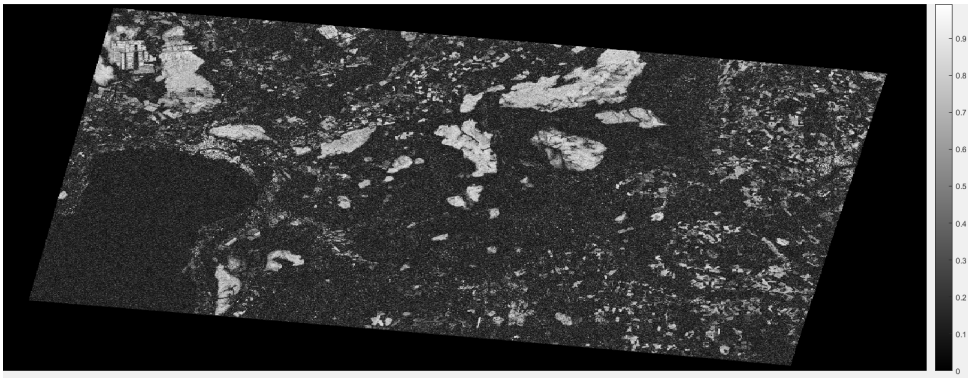

Figure 28: Terrain-corrected interferometric coherence of image pair 30^{th} Sept-06^{th} Oct, 2016 in VV polarization. The coherence scales from 0 to 1. Dark areas are indicating low coherence and bright areas indicating high coherence.

The *geographic latitude/longitude* is set as a default map projection in terrain correction operator. Coordinate Reference System (CRS) of the terrain corrected image is changed to EPSG-32635 (WGS/UTM zone 35) by using re-projection in SNAP. European Petroleum Survey Group (EPSG) keeps database of coordinate system information. It also provide documents on map projections. EPSG-32635 is used for implementing InSAR processing chain and will be used for backscattering chain in section 4.2. Image pixel is set to 20 m resolution by using re-sampling operator after performing re-projection as shown in Fig.29.

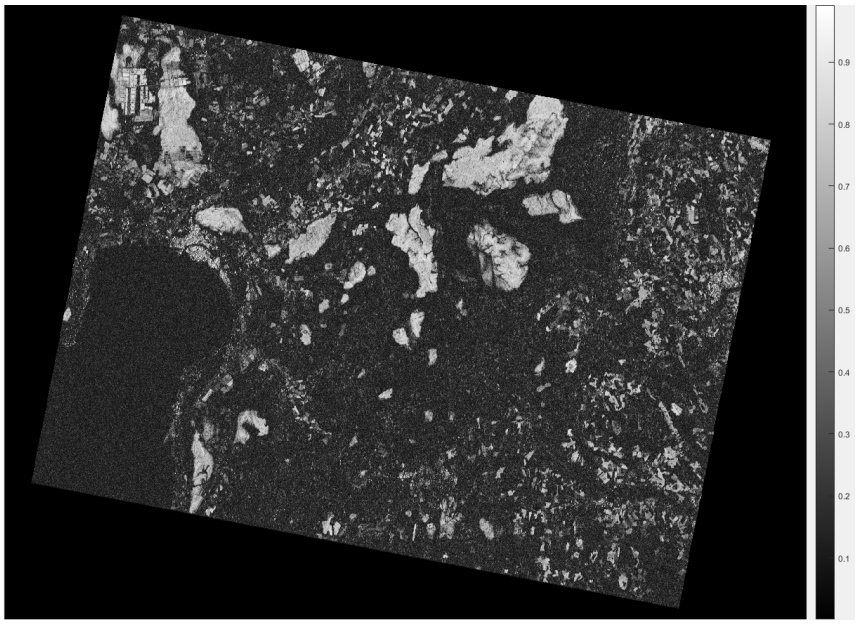

Figure 29: Re-projected and re-sampled interferometric coherence of image pair 30^{th} Sept-06^{th} Oct, 2016 in VV polarization. The coherence scales from 0 to 1. Dark areas are indicating low coherence and bright areas indicating high coherence.

The Fig.30 shows the subset of the re-projected and re-sampled interferometric coherence image.

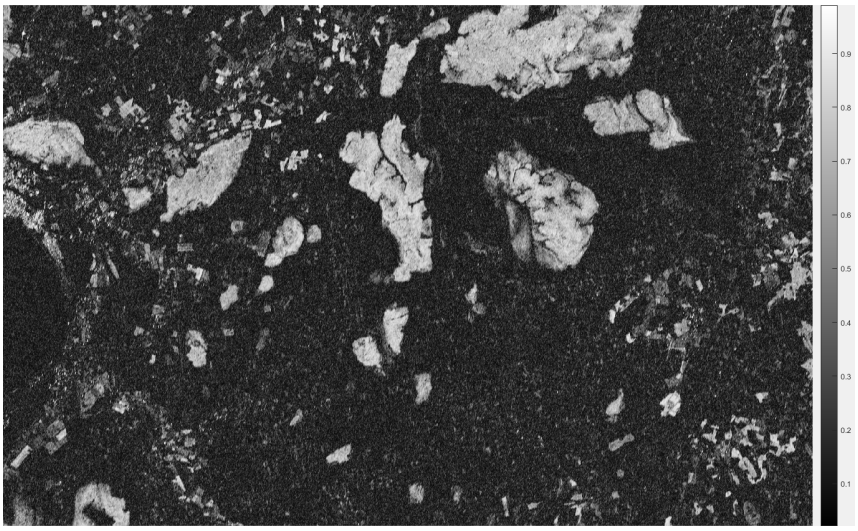

Figure 30: Subset of interferometric coherence of image pair 30^{th} Sept-06^{th} Oct, 2016 in VV polarization. The coherence scales from 0 to 1. Dark areas are indicating low coherence and bright areas indicating high coherence.

The subset is made by defining the geometric coordinates covering the test site. Geographic coordinates are provided in table 4.

	Geo Coordinates
North latitude bound	58.50
West longitude bound	24.50
South longitude bound	58.20
East longitude bound	25.45

Table 4: Geo-coordinates specification for study area.

The processing chain of interferogram formation depends on the software and the precise application but will include combination of steps shown in Fig.31.

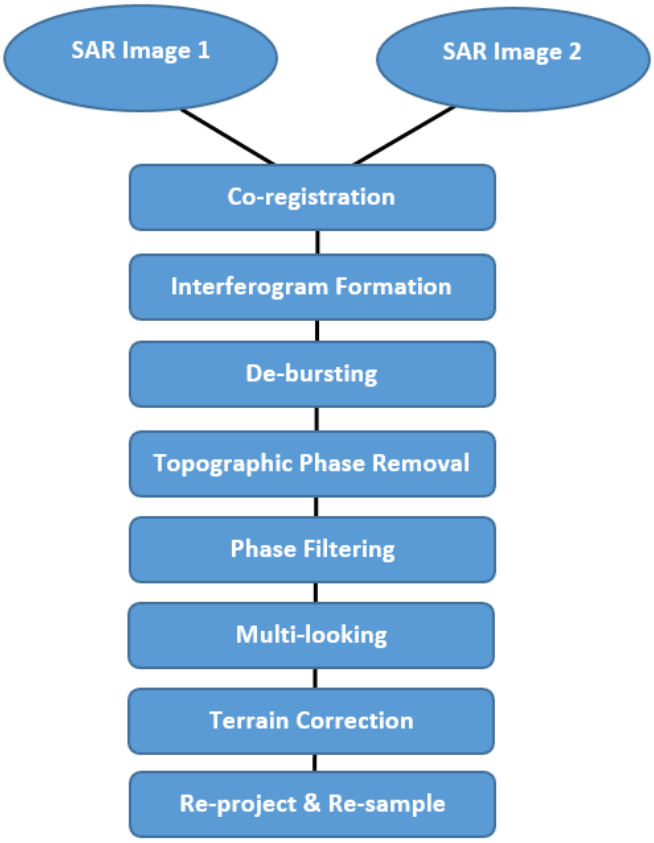

Figure 31: InSAR processing block diagram.

The Interferometric SAR image processing chain using SNAP graph builder is shown in Fig.32.

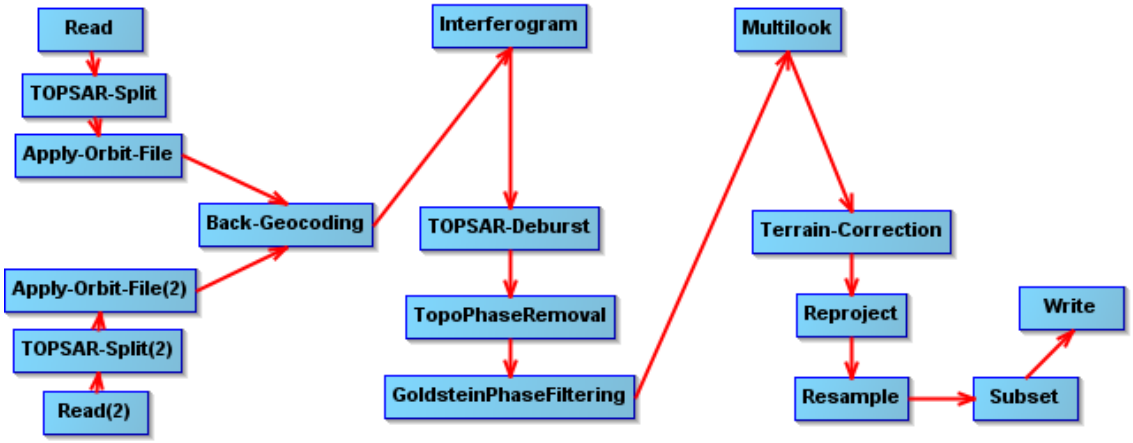

Figure 32: InSAR processing chain using SNAP.

4.2 Backscattering Processing Chain

Similarly, the set up of backscattering processing chain and its implementation on Sentinel-1 SAR image is presented in this section. A single SAR acquisition, acquired on 30^{th} of September from Sentinel-1A is used for processing chain. Our test area is located in the IW3 sub-swath as shown earlier in Fig.25.

Backscattering processing requires a single SLC product. TOPSAR splitting and orbit file is assigned before performing the calibration step as did with interferometric coherence processing chain. Calibration is performed on the SAR image to provide imagery with the radar backscattering values. While performing calibration in SNAP, beta0 output band is selected which will be used in terrain flattening step. Demarcation zones between the bursts are then removed by applying TOPS de-bursting shown in Fig.33. In backscattering intensity processing chain, only three bursts (4-6) from IW3 swath in VH polarization are used.

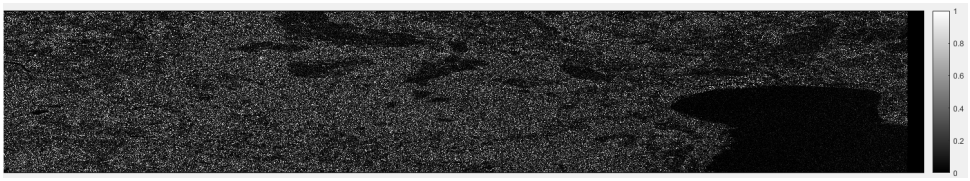

Figure 33: De-bursted backscatter image of 30^{th} Sept, 2016 in VH polarization. The relative backscattered value ranges from 0 to 1. Dark areas are indicating low backscattering and bright areas are indicating high backscattering.

Multi-looking is applied with 4 by 1 at range and azimuth respectively, shown in Fig.34. The process reduces noise taking the average of adjacent pixels in the SAR images.

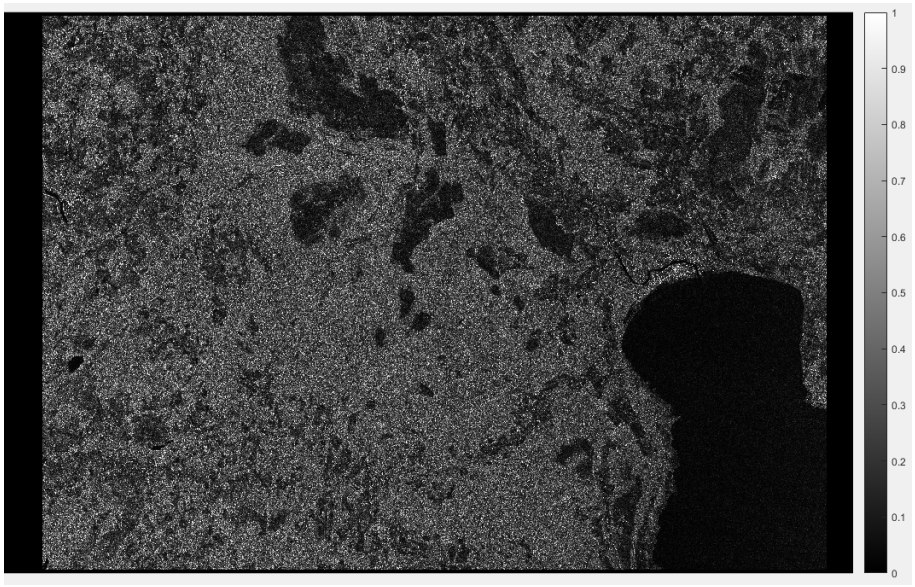

Figure 34: Multi-looked backscatter image of 30^{th} Sept,2016 in VH polarization. The relative backscattered value ranges from 0 to 1. Dark areas are indicating low backscattering and bright areas are indicating high backscattering.

Terrain flattening is a prior step before applying the terrain correction on multilooked image. The purpose of terrain flattening is to remove the radiometric variability influenced by terrain topography [69, 70]. Terrain correction uses DEM to remove geometric distortions by geocoding the image and produce a projected map as shown in Fig.35.

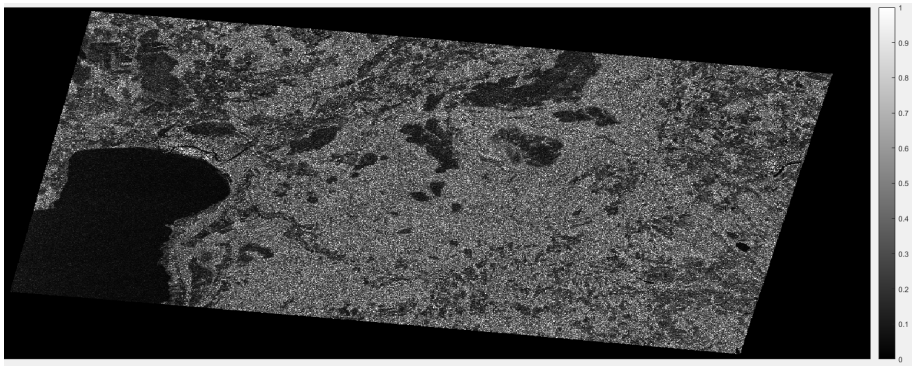

Figure 35: Terrain flattened and terrain-corrected backscatter image of 30^{th} Sept, 2016 in VH polarization. The relative backscattered value ranges from 0 to 1. Dark areas are indicating low backscattering and bright areas are indicating high backscattering.

SAR images are corrupted by a signal-dependent noise called speckle, that decreases the potentiality of images for human or automatic interpretation [71]. The degradation is caused by the radiation used, which is coherent in nature and its interaction with the roughness of the terrain. The median filter is applied to the image to mitigate the effect of speckle at the cost of reduced resolution shown in

Fig.36. The median filters are widely used in digital image processing, it removes the noise while preserving the image edges.

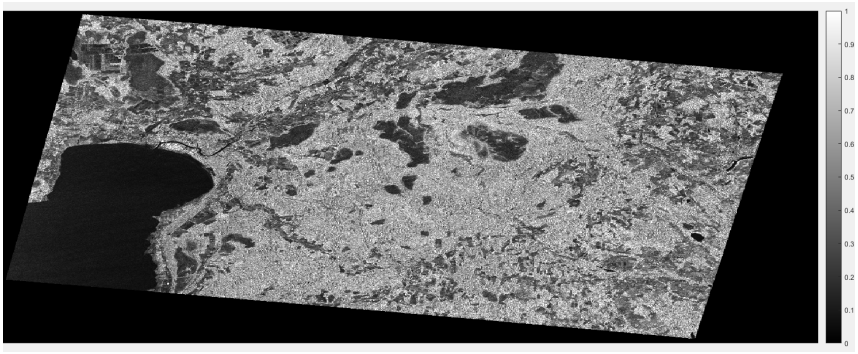

Figure 36: Speckle filtering of backscatter image of 30^{th} Sept, 2016 in VH polarization. The relative backscattered value ranges from 0 to 1. Dark areas are indicating low backscattering and bright areas are indicating high backscattering.

The CRS of the product is changed to EPSG-32635 (WGS/UTM zone 35) by using re-projection operator in SNAP tool as done previously with InSAR processing chain. Image pixel is set to 20 m resolution by using re-sampling operator. The re-sampled and re-projected image is shown in Fig.37.

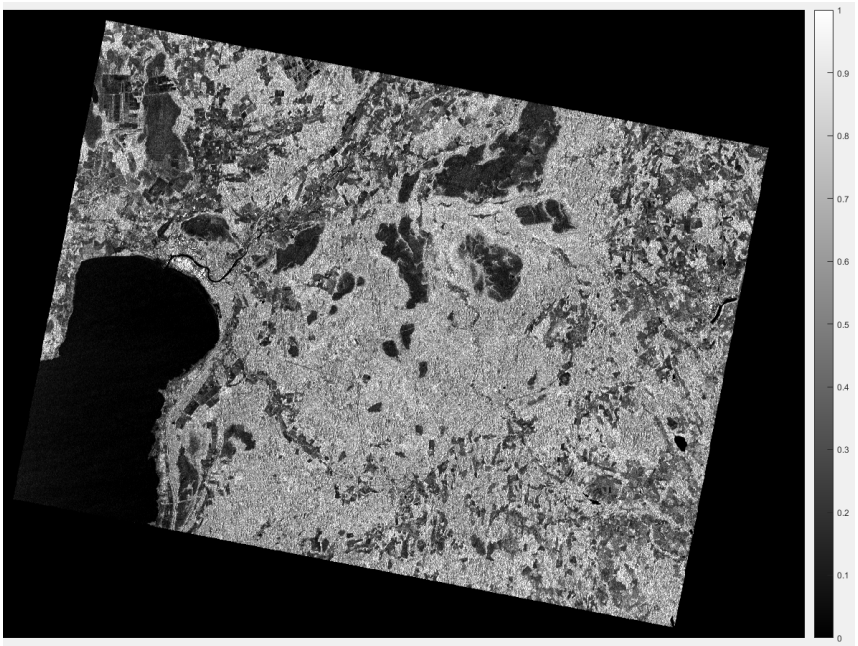

Figure 37: Re-projected and re-sampled backscatter Image of 30^{th} Sept, 2016 in VH polarization. The relative backscattered value ranges from 0 to 1. Dark areas are indicating low backscattering and bright areas are indicating high backscattering.

The Fig.38 shows the subset of the re-projected and re-sampled backscatter image.The subset is made by defining the geometric coordinates provided in the table 4.

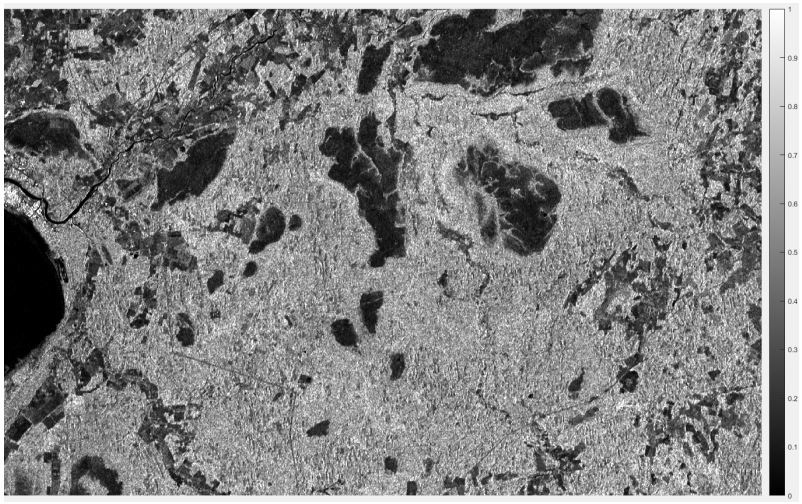

Figure 38: Subset of backscatter image of 30^{th} Sept, 2016 in VH polarization. The relative backscattered value ranges from 0 to 1. Dark areas are indicating low backscattering and bright areas are indicating high backscattering.

The block diagram of backscattering processing chain is shown in Fig.39.

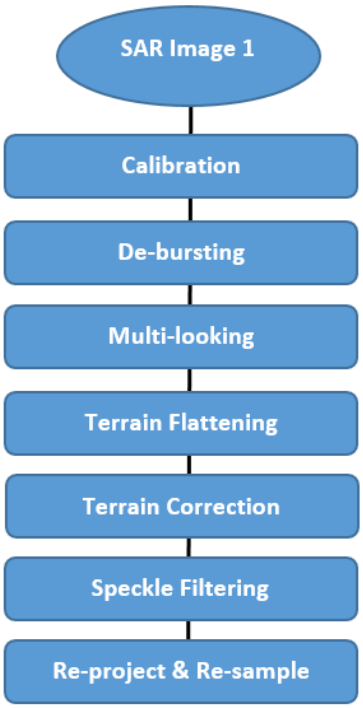

Figure 39: Backscattering intensity processing block diagram.

The backscattering SAR image processing chain using SNAP graph builder is shown in Fig.40.

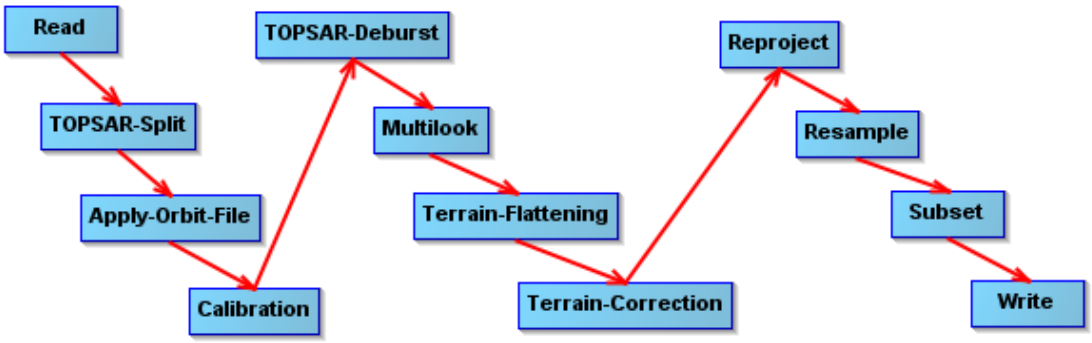

Figure 40: Backscattering intensity processing chain using SNAP.

4.3 Corine Map Processing

Corine Land Cover model (CLC2012) acquired for this study was in vector format (.shp file). It is converted to raster format in QGIS. The coordinate reference system of Corine map is converted from EPSG-3301 (Estonian Coordinates System of 1997) to EPSG-32635. The resolution is also set to 20 m. The re-projection and re-sampling of Corine map is done on SNAP shown in Fig.41.

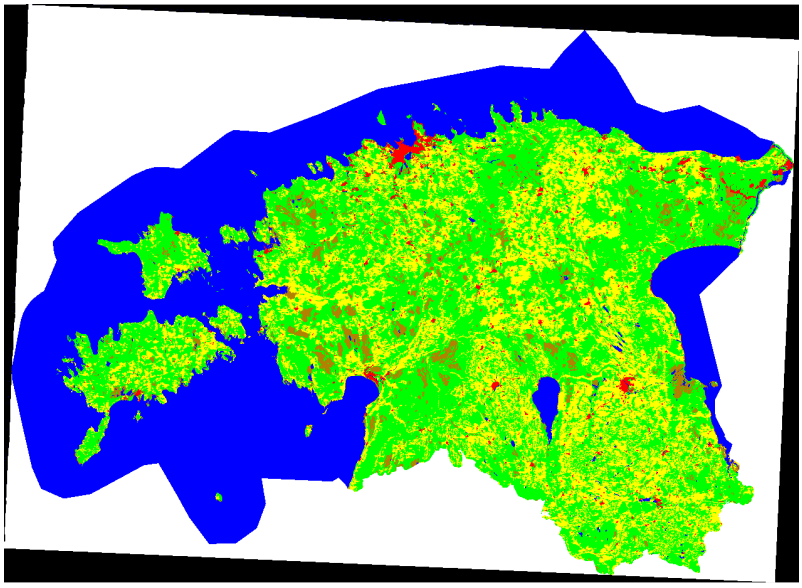

Figure 41: Re-projection and re-sampling of corine map over Estonia.

In this study, Corine map is used as a reference data. Initially, the Corine map contains 34 different classes.

4.4 Conversion to Major Classes

The 34 classes of Corine map are merged into 5 major classes using Matlab. Each class has been assigned with a number and colour. The class description is given in Table.5.

	Class Description	Colour
1	Artificial surfaces	Red
2	Field	Yellow
3	Forest	Green
4	Peat	Brown
5	Water	Blue

Table 5: Conversion of Corine map into 5 major classes.

In Matlab, grayscale image of Corine map is converted to RGB image shown in Fig.42. RGB image illustrates major portion of *Forest*, *Peat-land* and *Field* classes. *Urban* and *Water* has less representation in study area comparatively. RGB image is written to a Geotiff file with the same geographic raster reference as of the gray scale image. It will be further used with Sentinel-2A optical image in QGIS for feature extraction.

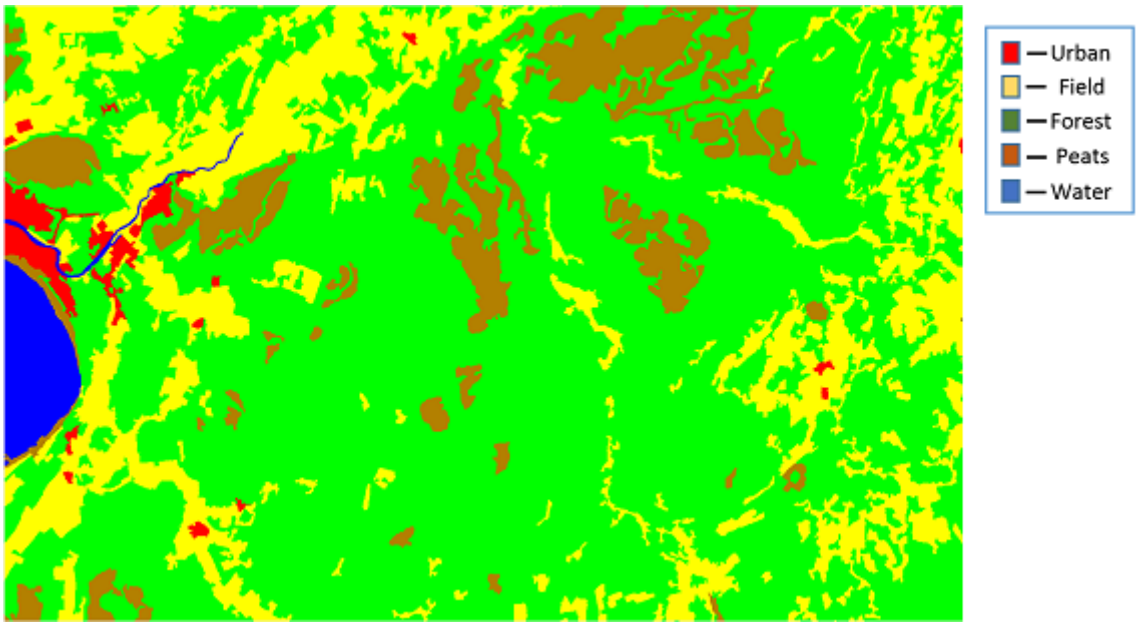

Figure 42: RGB image of converged corine map. Classes: Red- Urban; Yellow- Field; Green- Forest; Brown- Peat-land; Blue- Water.

5 Results

In this chapter, the interferometric coherence and backscattering intensity processed images have been shown using the processing chains set up in chapter.4. The classification results have been shown and explained using the developed classifying methodology. The results are also validated with the accuracy assessment method.

5.1 Interferometric Coherence

The interferometric coherence processing chain set up in chapter.4, has been applied on two SLC images of Sentinel-1 A/B. Two SAR images have been downloaded from the ESA Sentinels data archive. The two main SAR acquisitions used in this thesis are:

1. S1A-IW-SLC-1SDV-20160930T043407-20160930T043434-013277-015262-995E
2. S1B-IW-SLC-1SDV-20161006T043322-20161006T043349-002381-004063-E216

The basic parameters calculated for Sentinel-1 SAR acquisitions using SNAP operator (InSAR stack overview) are provided in Table.6.

Parameter	**File 1**	**File 2**
Type	SLC	SLC
Mst/Slv	Master	Slave
Acquisition	30Sep2016	06Oct2016
Track	80	80
Orbit	13277	2381
Bperp [m]	0.00	91.54
Btemp [days]	0.00	6.00
Modelled Coherence	1.0	0.92
Height Ambiguity [m]	Inf	172.10
Delta fDC [Hz]	0.00	2.77

Table 6: Basic parameters calculation for master/slave image.

The perpendicular baseline of 91.54 m and height ambiguity of 172.10 m is achieved with six days gap between the satellite acquisitions. As discussed in the section of InSAR fundamentals, suitable temporal and perpendicular baselines should be used in combination with the area of interest and available SAR data. In short temporal baseline, the scatterers do not change its position and structure and high coherent values are achieved. Perpendicular baselines also effect coherence and smaller baselines are advisable to use to achieve good coherence.

Using SNAP, the interferometric coherence image over the area of interest is shown in Fig.43. The interferometric coherence processing chain has been applied on two SLC images in VH polarization. The image contains bright as well as dark

areas. The bright areas are indicating high coherence values whereas dark areas indicating low coherence values. The classes including *Peat-land*, *Urban* and *Field* are represented by bright areas showing that scatterers do not change their structure and position. They have high coherent values between the two acquisitions with six days temporal baseline. However, *Forest* and *Water* have low coherence values and are represented by dark areas. The coherence value for *Water* is almost '0' as it changes position in a fraction of a second. The *Forest* also have low coherent values because *Forest* cover changes due to wind and other factors.

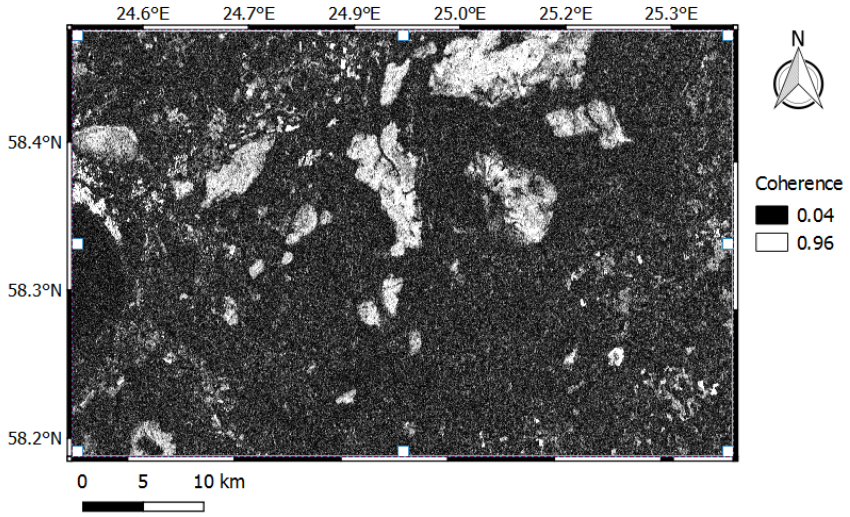

Figure 43: Interferometric coherence image in VH polarization. The coherence scales from 0 to 1. Dark areas are indicating low coherence and bright areas indicating high coherence.

In Fig.44, the histogram of interferometric coherence in VH polarization is shown. The coherence value ranges from 0.04 to 0.96. The distribution of classes is high between 0.1 and 0.3. However, some classes are distributed between 0.3 and 0.6 but their concentration is low.

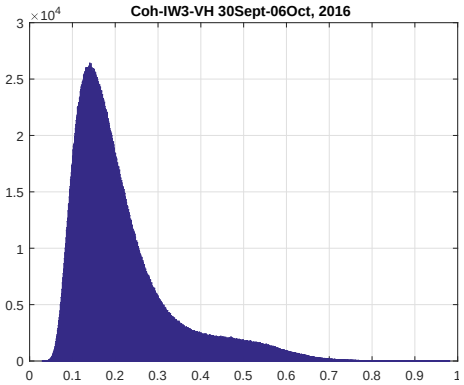

Figure 44: Histogram of interferometric coherence in VH polarization (30^{th} Sept-06^{th} Oct, 2016).

Similarly the interferometric coherence image over the area of interest is shown in Fig.45. The processing chain has been applied on two SLC images in VV polarization. The VV polarized image appears less noisy as compared to VH polarized image. *Peatland*, *Urban* and *Field* are represented by bright areas and have high coherent values, whereas, *Forest* and *Water* areas have low coherence values and are represented by dark areas.

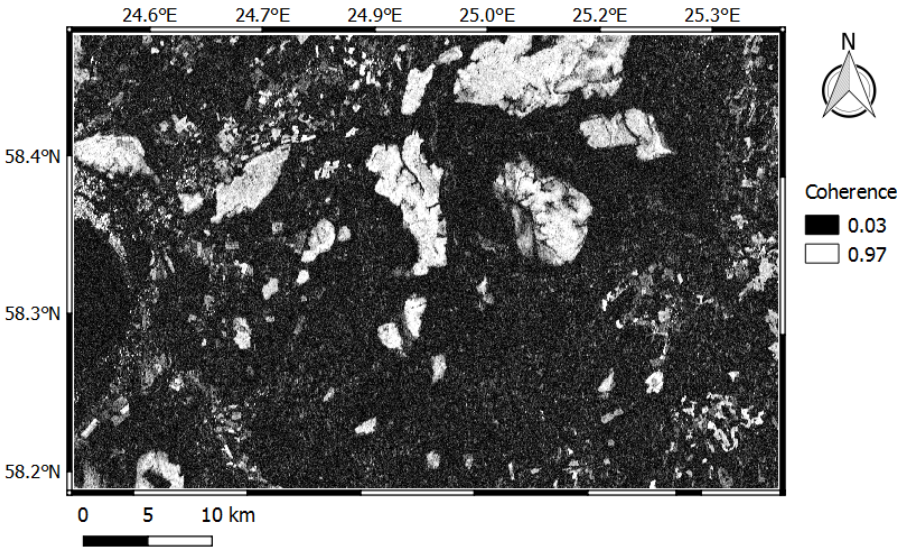

Figure 45: Interferometric coherence image in VV polarization. The coherence scales from 0 to 1. Dark areas are indicating low coherence and bright areas indicating high coherence.

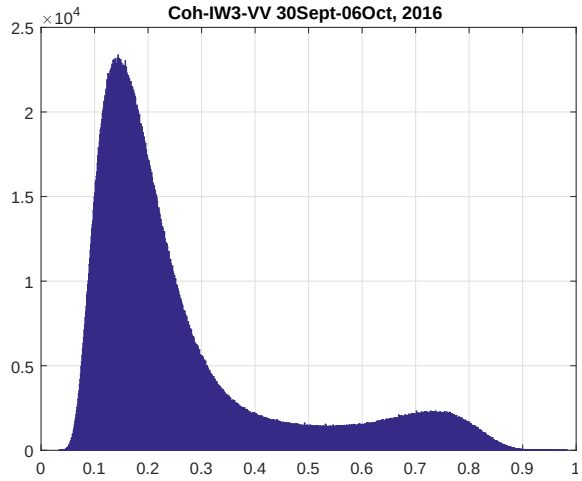

Figure 46: Histogram of interferometric coherence in VV polarization (30^{th} Sept-06^{th} Oct, 2016).

In Fig.46, the histogram of interferometric coherence in VV polarization is shown. The coherence value ranges from 0.03 to 0.97. The graph shows high distribution of

classes in low coherent values between 0.1 and 0.3. Compared to Fig.44, the graph shows continuity with low coherence values upto 0.85.

5.2 Backscattering Intensity

The backscattering intensity image over the area of interest is shown in Fig.47. The backscattering intensity processing chain has been applied on image acquired on 30^{th} September, 2016 in VH polarization. The image contains bright as well as dark areas. The intensity image is usually represented as gray scale image and intensity represents the reflected microwave from ground targets depending on various factors. These factors include the size, type, shape and structure of the target, moisture content, frequency and polarization of radar pulses. The areas with high reflectance are represented by bright areas and low reflectance is represented by dark areas. *Urban* has the high backscattering intensity and is represented by very bright area. The trees and other vegetation appear moderately bright in the image but its reflectance values are lower than *Urban*. The *Water* has '0' reflectance and is represented with dark area. The *Field* and *Peat-land* also have low reflectance values but *Peat-land* appears more dark as it might contain *Water* content to some extent.

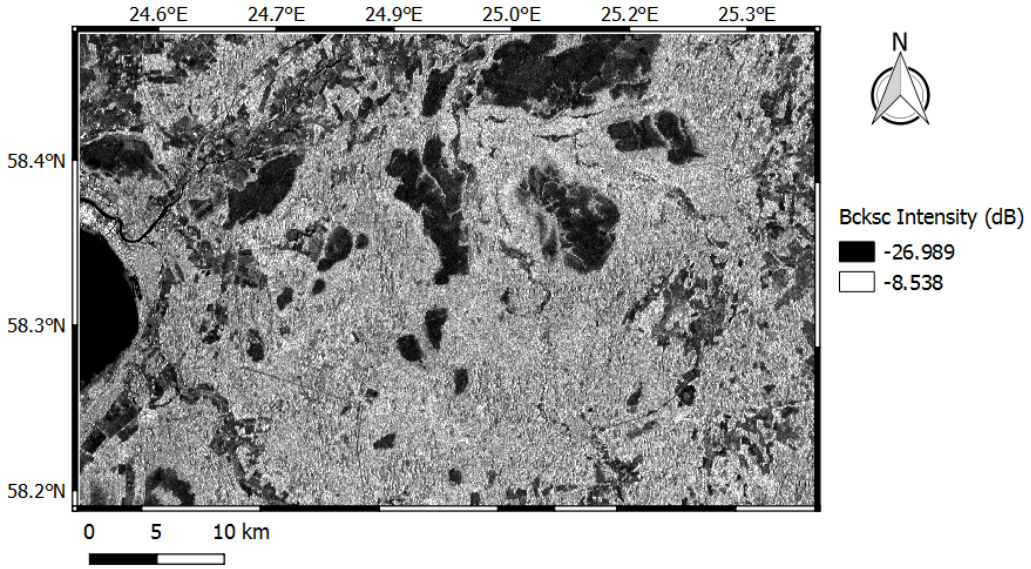

Figure 47: Backscattering intensity image in VH polarization. The relative backscattered value is converted to decibel (dB). Dark areas are indicating low backscattering and bright areas are indicating high backscattering.

The histogram of backscattered intensity in VH polarization is shown in Fig.48. The relative backscattered values are converted to decibels (dB). The histogram is representing the distribution of class data ranging from -26.98 dB to -8.54 dB. The class distribution is high between -17.0 dB and -14.0 dB.

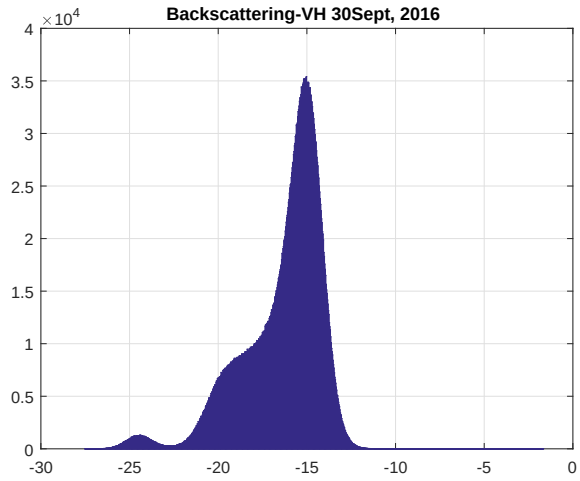

Figure 48: Histogram of backscattering intensity in VH polarization (30^{th} Sept, 2016).

Similarly the backscattering intensity image is shown in Fig.49. The backscattering intensity processing chain has been applied on SAR image acquired on 30^{th} September, 2016 in VV polarization. In VV polarized image, some more bright areas can be observed which can not be seen in VH polarized image. *Peat-land* appears less dark, *Forest* and vegetation area appears more dark comparatively in co-polarization.

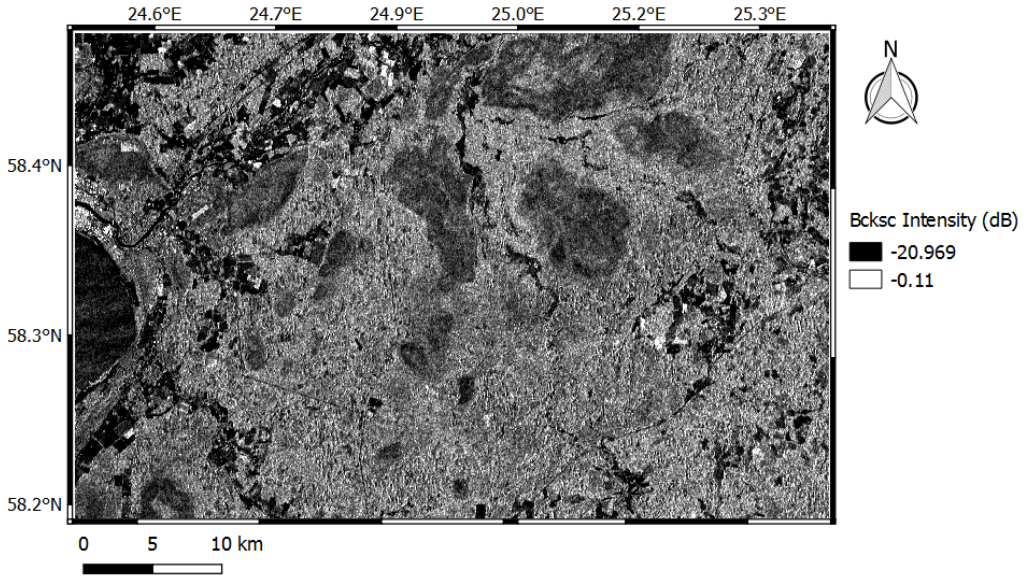

Figure 49: Backscattering intensity image in VV polarization. The relative backscattered value is converted to decibel (dB). Dark areas are indicating low backscattering and bright areas are indicating high backscattering.

In Fig.50, the histogram of backscattering intensity in VV polarization is shown. The graph shows one peak between -14.0 dB and -9.0 dB. All five classes are distributed within this range.

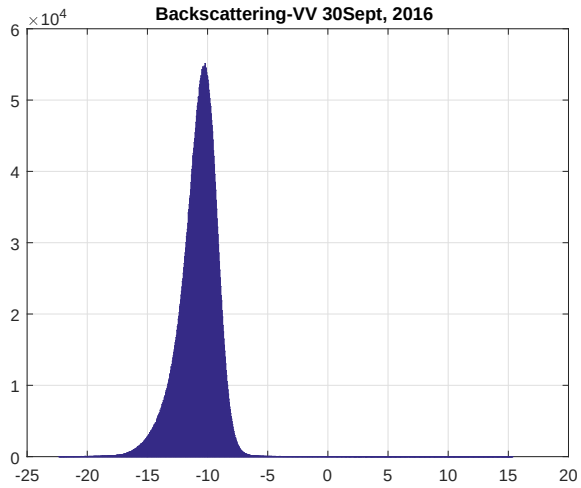

Figure 50: Histogram of backscattering intensity in VV polarization (30^{th} Sept, 2016).

In Fig.51, the intensity image over the area of interest is shown. The image was acquired on 06th October, 2016. The processing chain has been applied on the image in VH polarization. The VH polarized image is representing same features with dark and bright areas as shown in Fig.46.

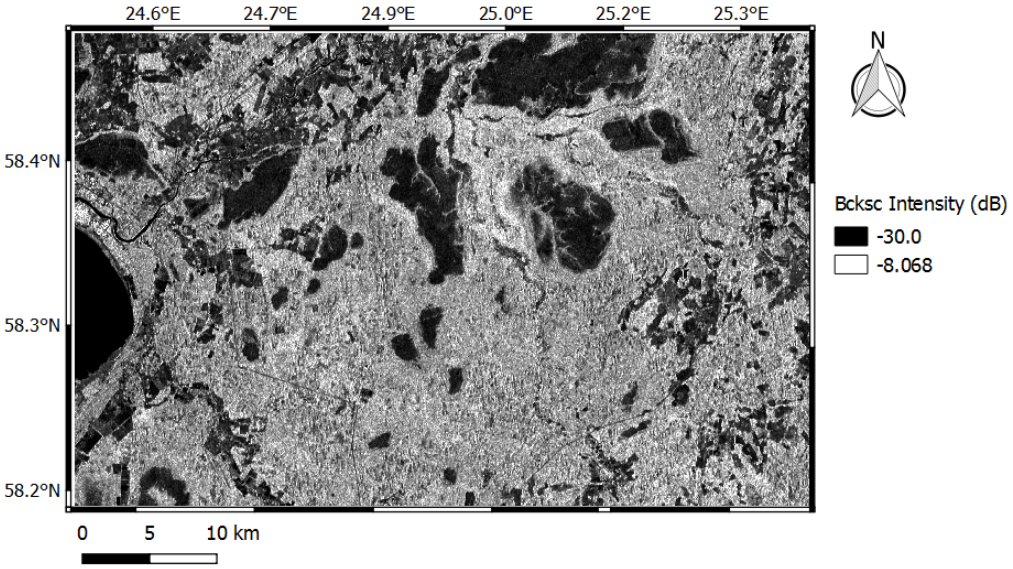

Figure 51: Backscattering intensity image in VH polarization. The relative backscattered value is converted to decibel (dB). Dark areas are indicating low backscattering and bright areas are indicating high backscattering.

In Fig.52, the histogram of backscattering intensity in VV polarization is shown. The graph scales from -30.0 to -8.07. The histogram shows three peaks at -27.0 dB, -19.0 dB and -16.0 dB respectively.

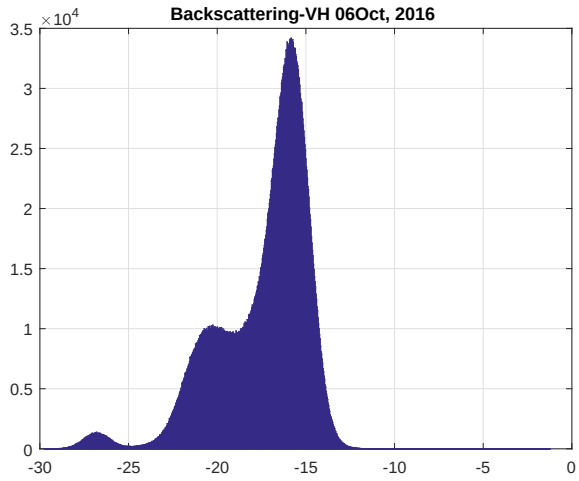

Figure 52: Histogram of backscattering intensity in VH polarization (06^{th} Oct, 2016).

Similarly the backscattering intensity image over the area of interest is shown in Fig.53. The backscattering intensity processing chain has been applied on image acquired on 06th October, 2016 in VV polarization. *Peat-land* appears less dark, *Forest* and vegetation area appears more dark comparatively in co-polarization as in the case of image acquired on 30th September, 2016.

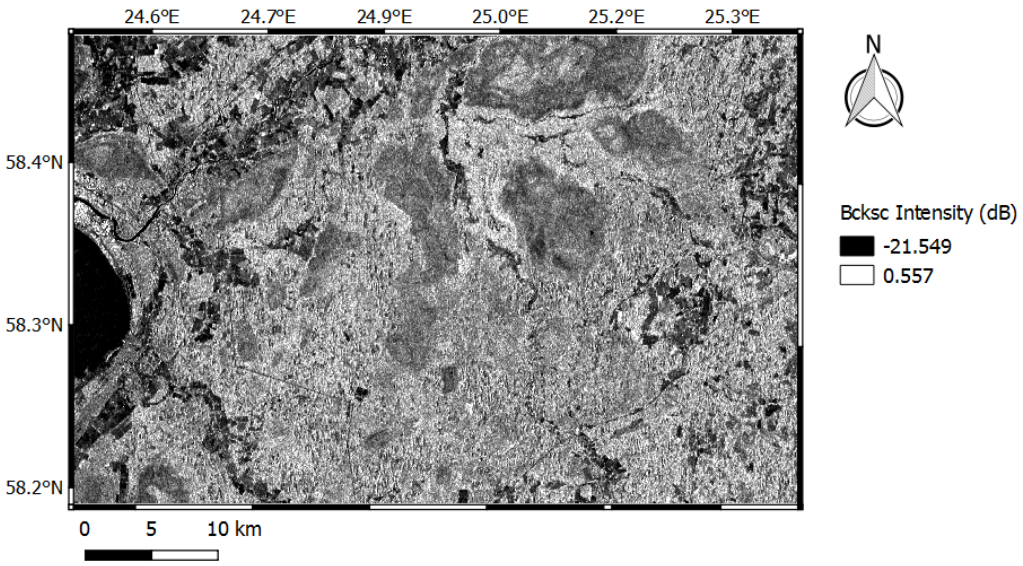

Figure 53: Backscattering intensity image in VV polarization. The relative backscattered value is converted to decibel (dB). Dark areas are indicating low backscattering and bright areas are indicating high backscattering.

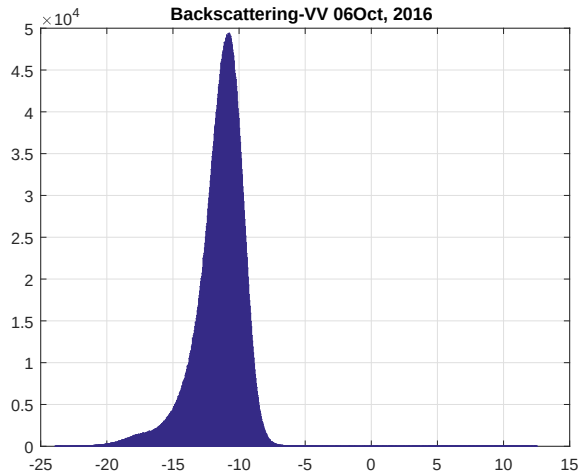

Figure 54: Histogram of backscattering intensity in VH polarization (06^{th} Oct, 2016).

In Fig.54, the histogram of backscattering intensity in VV polarization is shown. The histogram of both acquisitions (30^{th} sept-06^{th} oct, 2016) in VV polarization are same. Similarly, this graph shows one peak between -16.0 dB and -9.0 dB.

5.3 Land Cover Classification Results

In this section, results of land cover classification will be presented using supervised classification technique. KNN algorithm is utilised for generating classified land cover maps. The obtained results are verified with confusion matrix validation method.

The two Sentinel-1A/B SLC images were acquired on 30^{th} September,2016 and 06^{th} October, 2016 with a gap of six days. In this work, two parameters have been used for land cover classification using Sentinel-1 including interferometric coherence and backscattering intensity. Land cover mapping is performed using both parameters together and separately in both (VV,VH) polarizations with K-17 for kNN classifier.

The classified map obtained using coherence in co-pol (VV) and backscattering intensity in cross-pol (VH) is shown in Fig.55. The classified map shows five major classes as defined in the reference data. These five classes are as following: *Urban*, *Field*, *Forest*, *Peat-land* and *Water*. Representation of the *Forest* (tree and vegetation) class is large in the classified map. Mixture of classes is considered as misclassification. As it can be seen in Fig.55, compared with the reference data, classes are misclassified. Misclassification suppresses the class representation and affects the classification accuracy. Major portion of *Field* is mixed with *Forest*. *Urban* is misclassified with *Peat-land* and *Forest*. On the right bottom corner of map, *Field* area is mixed with *Peat-land*.

The confusion matrix is used as a classification validation method as shown in Table.7. The classification accuracy of 72.4% is obtained with interferometric coherence in co-pol and backscattering intensity in cross-pol. Confusion matrix is calculated by comparing the classified results with the CLC2012 reference data. Actual classification is represented by rows and predicted classification is represented by columns. Diagonal elements gives the percentage of accurately classified pixels

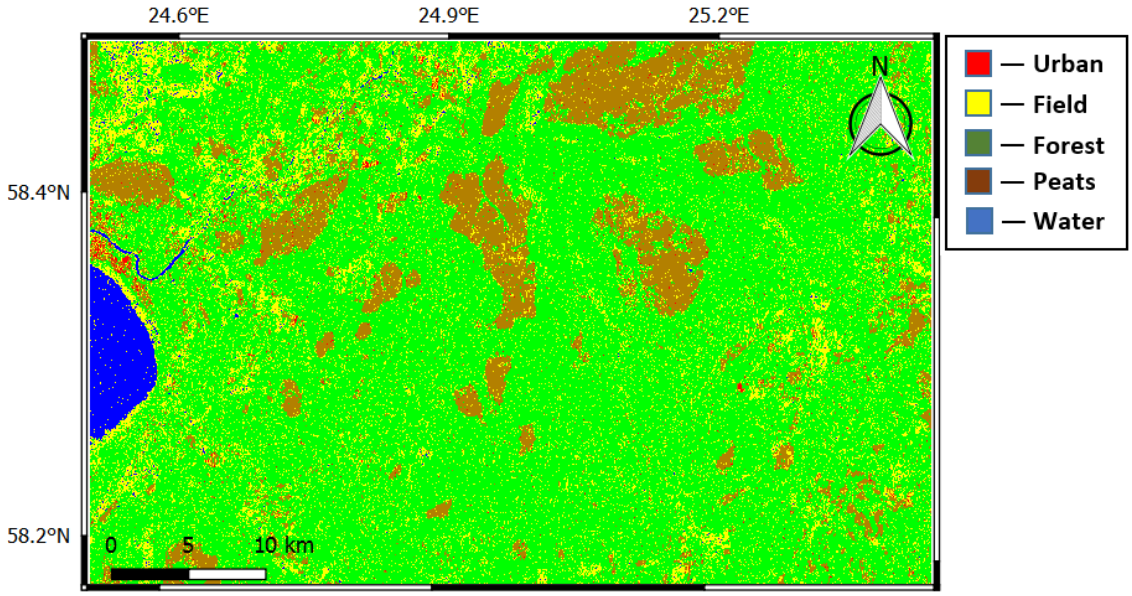

Figure 55: Classification results over Estonia using CohVV + bsVH. Classes: Red- Urban; Yellow- Field; Green- Forest; Brown- Peat-land; Blue- Water.

K-Nearest Neighbour							
	urban	field	forest	peatland	water	total	producer's accuracy
urban	**0.1**	0.3	0.6	0.3	0.0	1.3	**7.6**
field	0.2	**6.5**	11.2	2.5	0.2	20.6	**31.7**
forest	0.2	6.5	**57.3**	3.4	0.0	67.4	**85.2**
peatland	0.1	0.9	1.3	**6.7**	0.0	9.0	**75.0**
water	0.0	0.1	0.0	0.0	**1.8**	1.9	**92.4**
total	0.6	14.3	70.4	12.9	2.0		
user's accuracy	**21.0**	**45.7**	**81.4**	**52.1**	**87.0**		**72.4**

Table 7: (Coh-VV + bs-VH) confusion matrix.

according to class and rest of the elements are errors of omission and commission as discussed in section 2.3.4. *Forest* dominates with 57.3% accuracy. *Peat-land* and *Field* are of the same ratio with 6.7% and 6.5% respectively. User's and producer's accuracies for *Water* are high. *Urban* is the least accurately classified class with 0.1% accuracy.

The land classification map generated using coherence in cross-pol (VH) and backscattering intensity in co-pol (VV) is shown in Fig.56. *Forest* (tree and vegetation) class is largely represented in the classified map. In this case, classified map is produced with two parameters but with different polarizations. It is visually obvious from the map that classes are misclassified. Major portion of *Field* is mixed with *Forest* and top left corner shows misclassification with *Water*. *Urban* is misclassified

with *Peat-land* and *Forest* but it is more prominent as compared to previous results. *Water* is largely misclassified with both *Forest* and *Peat-land*.

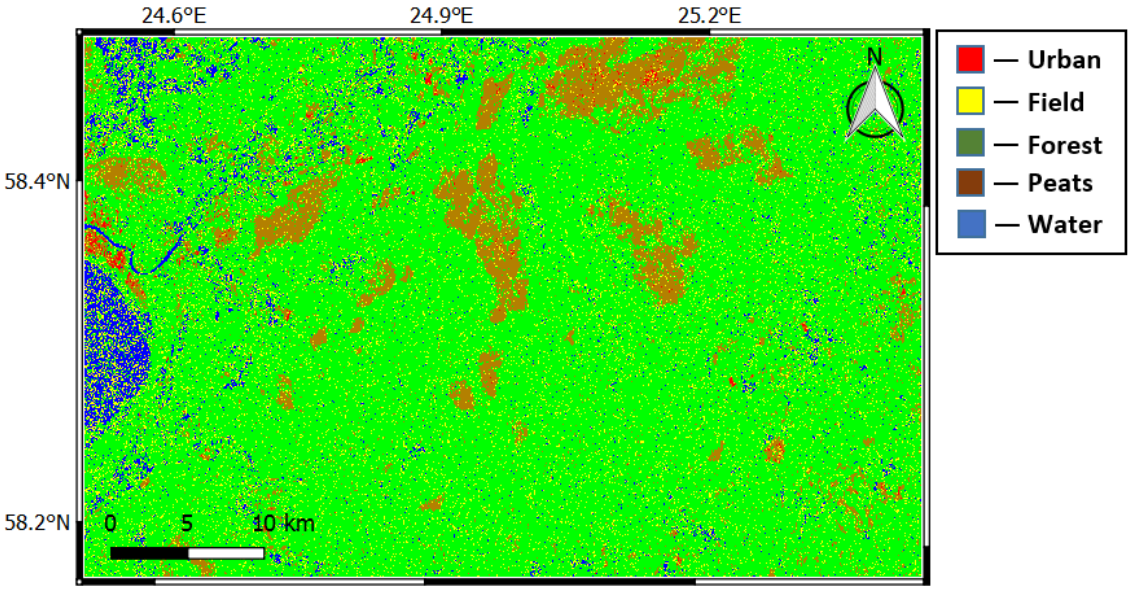

Figure 56: Classification results over Estonia using CohVH+bsVV. Classes: Red- Urban; Yellow- Field; Green- Forest; Brown- Peat-land; Blue- Water.

K-Nearest Neighbour							
	urban	field	forest	peatland	water	total	producer's accuracy
urban	**0.1**	0.1	0.7	0.4	0.0	1.3	**9.1**
field	0.0	**3.0**	13.6	1.7	2.2	20.5	**14.1**
forest	0.0	4.4	**60.1**	2.2	0.6	67.3	**89.2**
peatland	0.0	0.6	2.6	**5.5**	0.0	8.7	**61.7**
water	0.0	0.4	0.4	0.0	**1.2**	2.0	**59.5**
total	0.1	8.5	77.4	9.8	4.0		
user's accuracy	**38.2**	**34.2**	**77.7**	**56.1**	**27.8**		**69.7**

Table 8: (Coh-VH + bs-VV) confusion matrix.

The classification accuracy of 69.7% is obtained with interferometric coherence in cross-pol and backscattering intensity in co-pol shown in Table.8. *Forest* accuracy increases to 60.1%, whereas *Water* and *Field* accuracies decreases to 1.2% and 3.0% respectively.

In Fig.57, the classification accuracy of 68.1% is achieved with interferometric coherence in both (VH,VV) polarization. *Water* is completely misclassified with *Forest*. *Peat-land* is mixed with *Field* as well as with *Urban*.However, *Peat-land* is comparatively more clear and dominant in Coherence classified map.

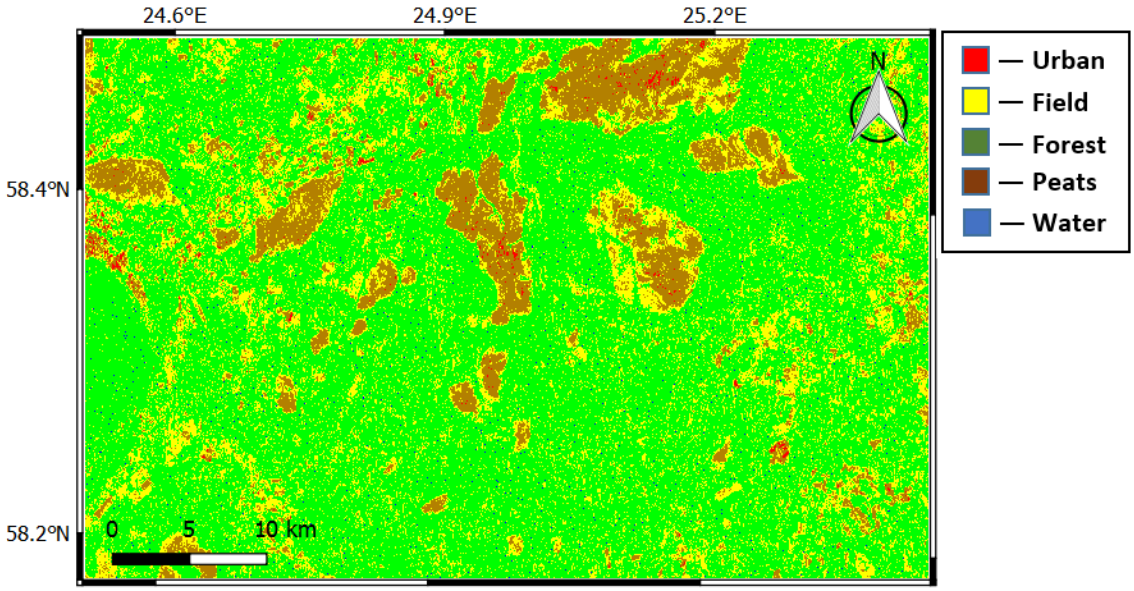

Figure 57: Classification results over Estonia using (VH+VV) coherence. Classes: Red- Urban; Yellow- Field; Green- Forest; Brown- Peat-land; Blue- Water.

The classification accuracy is reduced to 68.1% with interferometric coherence shown in Table.9. *Forest* accuracy decreases to 54.5%, whereas *Water* decreases to 0.0% accuracy. *Field* and *Peat-land* are increased to 7.3% and 6.2% respectively. User's and producer's accuracies for *Peat-land* increases to 62.8% and 70.0% respectively.

K-Nearest Neighbour							
	urban	field	forest	peatland	water	total	producer's accuracy
urban	**0.1**	0.5	0.4	0.3	0.0	1.3	**4.7**
field	0.1	**7.3**	11.4	2.0	0.0	20.8	**35.8**
forest	0.0	11.0	**54.5**	2.0	0.2	67.7	**81.0**
peatland	0.1	2.0	1.0	**6.2**	0.0	9.3	**70.0**
water	0.0	0.1	2.0	0.0	**0.0**	2.1	**0.7**
total	0.3	20.9	69.3	10.5	0.2		
user's accuracy	**22.0**	**35.6**	**79.0**	**62.8**	**5.6**		**68.1**

Table 9: Interferometric coherence (VH + VV) confusion matrix.

In Fig.58, the classification accuracy of 68.8% is achieved with backscattering intensity in both (VH,VV) polarization. *Water* is accurately classified. *Peat-land* and *Field* are mixed together. *Urban* area is entirely misclassified with *Forest*. On top left and bottom left corners, *Urban* is misclassified with *Field*.

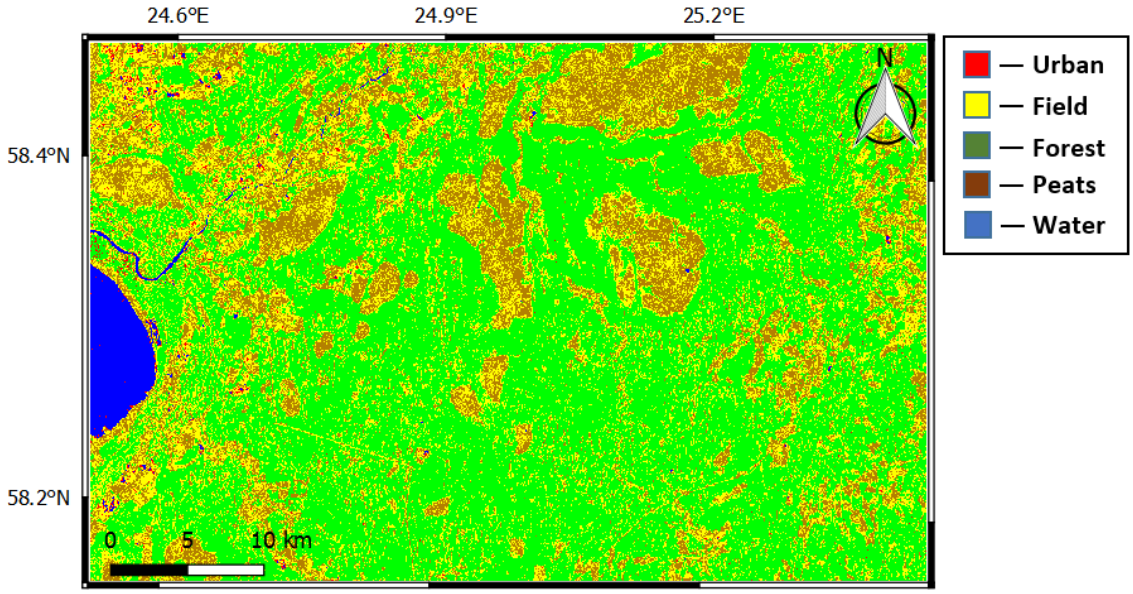

Figure 58: Classification results over Estonia using (VH+VV) backscatter. Classes: Red- Urban; Yellow- Field; Green- Forest; Brown- Peat-land; Blue- Water.

The classification accuracy of 68.8% is achieved with backscattering intensity shown in Table.10. *Forest* accuracy decreases to 53.0%, whereas *Water* accuracy increases to 1.8%. *Field* is increased to 8.9%. User's and producer's accuracies for *Water* increases to 91.5% and 92.6% respectively.

K-Nearest Neighbour							
	urban	field	forest	peatland	water	total	producer's accuracy
urban	**0.1**	0.5	0.6	0.3	0.3	1.8	**4.0**
field	0.3	**8.9**	4.0	7.3	0.1	20.6	**43.2**
forest	0.0	10.3	**53.0**	4.2	0.0	67.5	**78.4**
peatland	0.0	3.2	0.4	**5.3**	0.0	8.9	**59.2**
water	0.0	0.1	0.0	0.0	**1.8**	1.9	**92.6**
total	0.4	23.0	58.0	17.1	2.2		
user's accuracy	**11.8**	**38.8**	**91.4**	**31.0**	**91.5**		**68.8**

Table 10: Backscatter intensity (VH + VV) confusion matrix.

6 Conclusion

This study has been followed through with the purpose to examine the potential of single pair C-band InSAR dataset of Sentinel-1 in land cover monitoring. Sentinel-1A satellite was launched on 03^{rd} April, 2014. With the launch of Sentinel-1B on 25^{th} April, 2016, Sentinel-1 constellation is complete.

The selected area of interest (54.18 km x 35 km) is situated in south west of Estonia (58° 24' N, 25° E). Two Sentinel-1 SAR images were acquired with six days temporal baseline; 30^{th} September, 2016 from Sentinel-1A and 06^{th} October, 2016 from Sentinel-1B. Using SNAP, interferometric coherence and backscatter intensity processing chains have been set up and images are generated over specified area. The CLC2012 land cover model was acquired from Estonia and used as a reference data in our study. Sentinel-2A optical data was used additionally in combination with the reference data to extract the training samples using QGIS. The land cover classification maps were generated using supervised classification technique.

In this study, the overall accuracy achieved in south west of Estonia was between 68% and 73% using single pair C-band InSAR data of Sentinel-1 and kNN supervised classification method. Dammert et al. achieved an overall accuracy between 65% to 75% using three tandem pairs and unsupervised classification method [15]. Strozzi et al. achieved overall accuracy of 75% utilising 8 tandem pairs in Bern, 4 tandem pairs in Lozère and 6 tandem pairs in Tuusula [16]. Engdahl et al. achieved an overall classification accuracy for Helsinki metropolitan area was of 90% using 14 ERS-1/2 tandem InSAR pairs and two-stage hybrid classifier method for land cover classification [17]. These studies acquired time series of Tandem datasets with different temporal baselines. Dammert et al. used coherence images with multiple of 3 days temporal baseline over Hokmark area while the coherence images over Gothenburg area was of one day temporal difference [15]. Strozzi et al. used InSAR dataset with 3 days temporal baseline [16]. Engdahl et al. used InSAR datset with one day temporal baseline and achieved 90% accuracy [17]. In comparison to these studies, single pair dataset of Sentinel-1 with six days temporal baseline was used in our study which explains the reason to achieve 73% accuracy. Data availability with short temporal baselines are suitable for achieving high accuracy results in land cover classification as the number of reliably distinguishable classes is larger [11].

The achieved land cover classification maps shows that short temporal baselines and combination of interferometric coherence with backscattering intensity provides more information about the land as compared to single feature usage. The perpendicular baseline of 91.54 m and height ambiguity of 172.10 m is achieved with Sentinel-1 single pair data. It is advisable to use suitable temporal and perpendicular baselines in combination with the area of interest and available SAR data as discussed in section 5.1. With short temporal baselines, the ground scatterers do not change their structure and position except water which changes its position in a fraction of second, that is why the coherent values are low for water. Moreover, short perpendicular baselines must be used to achieve high coherency.

The overall classification accuracy of 73% obtained with single pair C-band InSAR data of six days temporal baseline and KNN supervised classification technique, can be

further improved by using PolSAR technique. Instead of employing InSAR technique and single pair dataset, results can be improved with time series of dataset with PolSAR and different supervised and unsupervised classification methods. Antropov et al. achieved an overall accuracy of 82.6% in western Finland using PolSAR and supervised classification including PNN and maximum likelihood [72]. The study was conducted with ALOS datasaet in L-band but the techniques and methods are the same as used in this study.

In future, the launch of Sentinel-1C and 1D satellites in 2021 onwards would be a remarkable addition in the Sentinel-1 constellation. The Sentinel-1 constellation would be able to provide much better classification results in land cover mapping with shorter temporal baselines and time series of dataset.

References

[1] Di Gregorio, A. Land cover classification system: *Classification concepts and user manual: LCCS. Rome: FAO Publishing Management Service (2005). ISBN:92-5-104216-0.*

[2] Aspinal, R.J, and Hill, M.J (eds). Land use change: *Science, Policy and Management. CRC Press, Taylor & Francis: Boca Raton, FL. (2008). ISBN:978-1-4200-4296-2.*

[3] Feranec, J., Hazeu, G.W., Christensen, S. and Jaffarain, G. Corine land cover change detection in Europe (case studies of the Netherlands and Slovakia). *Land Use Policy (2007), 24(1), pp.234-247.*

[4] Friedl, M.A., Sulla-Menashe, D., Tan, B., Schneider, A., Ramankutty, N., Sibley, A. and Huang, X. MODIS collection 5 global land cover: algorithm refinements and characterization of new datasets. *Remote Sensing of Environment. (2010), Vol.114, pp. 168-182. DOI:10.1016/j.rse.2009.08.016.*

[5] Congalton, R.G., Gu, J., Yadav, K., Thenkabail, P. and Ozdogan, M. Global land cover mapping: a review and uncertainty analysis. *Remote Sensing. (2014), Vol.6, pp. 12070-12093. DOI:10.3390/rs61212070.*

[6] Lonpege, N., Rakwatin, P., Isoguchi, O., Shimada, M., Uryu, Y., and Yulianto, K. Assessment of ALOS PALSAR 50 m orthorectified FBD data for regional land cover classification by support vector machines. *IEEE Transactions on Geoscience and Remote Sensing, (2011), Vol.49, No.6, pp.2135-2150. ISSN:0196-2892. DOI:10.1109/TGRS.2010.2102041.*

[7] Niu, X. and Ban, Y. Multi-temporal RADARSAT-2 polarimetric SAR data for urban land-cover classification using an object-based support vector machine and a rule-based approach. *International Journal of Remote Sensing, (2013), Vol.34, No.1, pp.1-26. ISSN:0143-1161. DOI:10.1080/01431161.2012.700133.*

[8] Balzter, H., Cole, B., Thiel, C. and Schmullius, C. Mapping corine land cover from Sentinel-1A SAR and SRTM digital elevation model data using random forests. *Mdpi. Remote Sensing, (2015), Vol.7, No.11, pp.14876-14898. DOI:10.3390/rs71114876.*

[9] Torres, R., Snoeij, P., Geudtner, D., Bibby, D., Davidson, M., Attema, E., Potin, P., Rommen, B., Floury, N., Brown, M., Traver, I.N., Deghaye, P., Duesmann, B., Rosich, B., Miranda N., Bruno C., L'Abbate M., Croci R., Pietropaolo. A., Huchler, M. and Rostan, F. GMES Sentinel-1 mission. *Remote Sensing of Environment, (2012), Vol.120, pp.9-24. DOI:10.1016/j.rse.2011.05.028.*

[10] Roy, D.P., Wulder, M.A., Loveland, T.R., Woodcock, C.E., Allen, R.G., Anderson, M.C., Helder, D., Irons, J.R., Johnson, D.M., Kennedy, R., Scambos, T.A., Schaaf, C.B., Schott, J.R., Sheng, Y., Vermote, E.F., Belward, A.S.,

Bindschadler, R., Cohen, W.B., Gao, F., Hipple, J.D., Hostert, P., Huntington, J., Justice, C.O., Kilic, A., Kovalskyy, V., Lee, Z.P., Lymburner, L., Masek, J.G., McCorkel, J., Shuai, Y., Trezza, R., Vogelmann, J., Wynne, R.H. and Zhu, Z. Landsat-8: Science and product vision for terrestrial global change research.In: *Remote Sensing of Environment, (2014), Vol.145, pp.154-172. DOI:10.1016/j.rse.2014.02.001.*

[11] Engdahl, M. (2013). Doctoral Dissertation. In: *Multitemporal InSAR in land-cover and vegetation mapping.*

[12] Lillesand, M.T, Kiefer, R.W. and Chipman, J.W. *Remote Sensing and image interpretation (5^{th} ed.). Hoboken, NJ: Wiley (2004). ISBN: 9780470052457.*

[13] Colwell, R.N. Manual of remote sensing. *Manual of Remote Sensing (2^{nd} ed.). Publisher: American Society of Photogrammetry (1983). ISBN: 9780937294413.*

[14] Aggarwal, S.(2004). Principles of Remote Sensing. In: *Satellite Remote Sensing and GIS Applications in Agricultural Meteorology. pp.23-38.*

[15] Dammert, P.B.G, Askne, J.I.H and Kühlmann, S. Unsupervised segmentation of multitemporal interferometric SAR images.In: *IEEE Transactions on Geoscience and Remote Sensing, (1999), Vol.37, No.5, pp.2259-2271. ISSN:0196-2892. DOI:10.1109/36.789622.*

[16] Strozzi, T., Dammert, P.B.G, Wegmüller, U., Martinez, J.-M. and Askne, J.I.H. Landuse mapping with ERS SAR interferometry.In: *IEEE Transactions on Geoscience and Remote Sensing, (2000), Vol.38, No.2, pp.766-775. ISSN:0196-2892. DOI:10.1109/36.842005.*

[17] Engdahl, M.E. and Hyyppä, J.M. Land cover classification using multitemporal ERS-1/2 InSAR data.In: *IEEE Transactions on Geoscience and Remote Sensing, (2003), Vol.41, No.7, pp.1620-1628. ISSN:0196-2892. DOI:10.1109/TGRS.2003.813271.*

[18] Ferretti, A., Monti-Guarnieri, A., Prati, C. and Rocca, F. InSAR principles: guidelines for SAR interferometry processing and interpretation . *TM-19. (2007), ISSN: 1013-7076.*

[19] Sandia National Laboratories CONTRIBUTORS. Synthetic aperture radar, (2017), http://www.sandia.gov/radar/what_ is_ sar/, accessed 03-August-2017

[20] Henderson, F.M, and Lewis, A.J. Principles and applications of imaging radar: *Manual of Remote Sensing (3^{rd} ed.). Wiley (1998). ISBN:978-0471294061.*

[21] ESA Earth Online CONTRIBUTORS. Sentinel-1 mission, (2000-2017), https://earth.esa.int/web/guest/missions/esa-operational-eo-missions/sentinel-1, accessed 15-August-2017

[22] ESA Sentinel Online CONTRIBUTORS. Acquisition modes, (2000-2017), https://sentinel.esa.int/web/sentinel/user-guides/sentinel-1-sar/acquisition-modes, accessed 20-May-2017

[23] ESA Sentinel Online CONTRIBUTORS. Incidence angle, (2000-2017), https://earth.esa.int/handbooks/asar/CNTR5-5.html, accessed 20-May-2017

[24] Raney, R.K., Freeman, T., Hawkins, R.W. and Bamler, R. A plea for radar brightness. In: *IEEE. International Geoscience and Remote Sensing Symposium (IGARSS), (1994), pp.1090-1092. ISSN:0-7803-1497-2. DOI:10.1109/IGARSS.1994.399352.*

[25] Weeks, R.J., Smith, M., Pak, K., Li, W.H., Gillespie, A. and Gustafson, B. Surface roughness, radar backscatter, and visible and near-infrared reflectance in Death Valley, California. In: *Journal of Geophysical Research, (1996), Vol.101, No. E10, pp.23,077-20,090. DOI:10.1029/96JE01247.*

[26] radartutorial.eu CONTRIBUTORS. Image of side-looking radar. Publisher: Christian Wolff, (2008), http://www.radartutorial.eu/20.airborne/ab06.en.html, accessed 17-May-2017

[27] ESA Sentinel Online CONTRIBUTORS. Single look complex, (2000-2017), https://sentinel.esa.int/web/sentinel/user-guides/sentinel-1-sar/resolutions/level-1-single-look-complex, accessed 20-May-2017

[28] ESA Sentinel Online CONTRIBUTORS. Level-1 SLC products, (2000-2017), https://sentinel.esa.int/web/sentinel/technical-guides/sentinel-1-sar/products-algorithms/level-1-algorithms/single-look-complex, accessed 17-July-2017

[29] ESA Earth Online CONTRIBUTORS. Image of speckle filtering, (2000-2017), https://earth.esa.int/web/guest/missions/esa-operational-eo-missions/ers/instruments/sar/applications/radar-courses/content-3/-/asset_publisher/mQ9R7ZVkKg5P/content/radar-course-3-temporal-averaging, accessed 17-May-2017

[30] ESA Earth Online CONTRIBUTORS. Image interpretation: Speckle filtering, (2000-2017), https://earth.esa.int/web/guest/missions/esa-operational-eo-missions/ers/instruments/sar/applications/radar-courses/content-3/-/asset_publisher/mQ9R7ZVkKg5P/content/radar-course-3-image-interpretation-tone, accessed 17-May-2017

[31] ESA earthnet Online CONTRIBUTORS. Range doppler algorithm, (2014), http://envisat.esa.int/handbooks/asar/CNTR2-6-1-2-3.html, accessed 17-May-2017

[32] Cumming, I.G. and Bennett, J.R. Digital processing if SEASAT SAR data. In: *Acoustics, Speech, and Signal Processing, IEEE International Conference on ICASSP '79., (1979). DOI:10.1109/ICASSP.1979.1170630.*

[33] Rogers, A.E.E., and Ingalls, R.P. Venus: Mapping the surface reflectivity by radar interferometry.In: *Science, (1969), Vol.165, No.3895, pp.797-799. DOI: 10.1126/science.165.3895.797.*

[34] Graham, L.C. Synthetic interferometer radar for topographic mapping. In: *Proceedings of the IEEE, (1974), Vol.62, No.06, pp.763-768. 10.1109/PROC.1974.9516.*

[35] Zebker, H.A., and Goldstein, R.M. Satellite radar interferometry: Two-dimensional phase unwrapping. In: *Radio Science, (1986), Vol.91, No.B5, pp.4993-4999. DOI: 10.1029/JB091iB05p04993.*

[36] Goldstein, R.M., Zebker, H.A., and Werner, C.L. Topographic mapping from interferometric synthetic aperture radar observations. In: *Journal of Geophysical Research, (1988), Vol.23, No.04, pp.713-720. DOI: 10.1029/RS023i004p00713.*

[37] Duchossois, G., and Martin, P. ERS-1 and ERS-2 Tandem operations. *Tech. Rep. ESA Bulletin Nr. 83, Directorate for Observation of the Earth and its Environment, ESA, Paris, (1995).*

[38] Simard, M., Hensley, S., Lavalle, M., Dubayah, R., Pinto, N. and Hofton, M. An empirical assessment of temporal decorrelation using the uninhabited aerial vehicle synthetic aperture radar over forested landscapes. In: *Mdpi. Remote Sensing, (2012),4, pp.975-986. ISSN: 2072-4292. DOI:10.3390/rs4040975.*

[39] Rodriguez-Marek, E. and Martin, J.M. Theory and design of interferometric synthetic aperture radars. In: *IEE Proceedings F - Radar and Signal Processing, (1992), Vol.139, No.2, pp.147-159. ISSN: 0956-375X. DOI:10.1049/ip-f-2.1992.0018.*

[40] Li, F.K. and Goldstein, R.M. Studies of multibaseline spaceborne interferometric synthetic aperture radars. In: *IEEE Transactions on Geoscience and Remote Sensing, (1990), Vol.28, No.1, pp.88-97. ISSN: 0196-2892. DOI:10.1109/36.45749.*

[41] Richards, J.A. *Remote Sensing with Imaging Radar (2009). ISSN: 1860-4862, DOI: 10.1007/978-3-642-02020-9.*

[42] Researchgate CONTRIBUTORS. Types of InSAR, (2017), https://www.researchgate.net/publication/312383304_ Towards_ the_ operational_ generation_ of_ Advanced-DInSAR_ time-series_ products_ suited_ for_ the_ integration_ into_ seismic_ hazard_ assessments/figures, accessed 27-May-2017

[43] European Space Agency. *InSAR principles: Guidelines for SAR interferometry prcessing and interpretation (2007).*

[44] Moreira, J., Schwabisch, M., Fornaro, G., Lanari, R., Bamler, R., Just, D., Steinbrecher, U., Breit, H., Eineder, M., Franceschetti, G., Geudtner, D., and Rinkel, H. X-SAR interferometry: first results. In: *IEEE Transactions on Geoscience and Remote Sensing, (1995), Vol.33, No.04, pp.950-956. ISSN: 0196-2892. DOI: 10.1109/36.406681.*

[45] Rocca, F., Prati, C., and Ferretti, A. An overview of SAR interferometry, (2014). On: *ESA Earthnet Online.* http://earth.esa.int/workshops/ers97/program-details/speeches/rocca-et-al/, accessed 08-June-2017

[46] Prati, C., Rocca, F., Guarnieri, A.M., and Damonti, E. Seismic migration for Sar focusing: interferometrical applications. In: *IEEE Transactions on Geoscience and Remote Sensing, (1990), Vol.28, No.04, pp.627-640. ISSN: 0196-2892. DOI: 10.1109/TGRS.1990.572968.*

[47] Zebker, H.A., and Villasenor, J. Decorrelation in interferometric radar echoes. In: *IEEE Transactions on Geoscience and Remote Sensing, (1992), Vol.30, No.05, pp.950-959. ISSN: 0196-2892. DOI: 10.1109/36.175330.*

[48] Sokal, R. Classification: purposes, principles, progress, prospects. In: *Science, (1974), Vol.185, No.4157, pp.1115-1123. DOI: 10.1126/science.185.4157.1115.*

[49] Richards, J.A. *Remote sensing digital image analysis: An introduction (second edition) (1993).*

[50] Alpin, P., and Atkinson, P.M. Predicting missing field boundaries to increase per-field classification accuracy. In: *Photogrammetric Engineering and Remote Sensing, (2004), Vol.70, No.01, pp.141-149. ISSN: 0099-1112.*

[51] Madhura, M. and Venkatachalam, S. Comparison of Supervised Classification Methods On Remote Sensed Satellite Data: An application in Chennai, south India. In: *International Journal of Science and Research (IJSR), (2015), Vol.04, No.02, pp.1407-1411. ISSN: 2319-7064.*

[52] Lu, D. and Weng, Q. A survey of image classification methods and techniques for improving classification performance. In: *IEEE. International Journal of Remote Sensing, (2007), pp.823-870. DOI:10.1080/01431160600746456.*

[53] Theodoridis, S., Pikrakis, A., Koutroumbas, K., and Cavouras, D. *Introduction to pattern recognition: Matlab approach (first edition).* Burlington, MA: Academic Press, (2010). ISBN: 9780123744869.

[54] Arora, M.K., Narsimham, G., and Mohanty, B. Neural network approach for the classification of remotely sensed data. In: *Asian Pacific Remote Sensing and GIS Journal, (1998), pp.11-18.*

[55] Jin, H., Stehman, S.V., and Mountrakis, G. Assessing the impact of training sample selection on accuracy of an urban classification: A case study in Denver,

Colorado. In: *International Journal of Remote Sensing, (2014), Vol.35, No.06, pp.2067-2081. DOI: 10.1080/01431161.2014.885152*

[56] Hammond, T.O., and Verbyla, D.L. Optimistic bias in classification accuracy assessment. In: *International Journal of Remote Sensing , (1996), Vol.17, No.06, pp.1261-1266. DOI: 10.1080/01431169608949085*

[57] Verbyla, D.L., and Hammond, T.O. Conservative bias in classification accuracy assessment due to pixel-by-pixel comparison of classified images with reference grids. In: *International Journal of Remote Sensing, (1995), Vol.16, No.03, pp.581-587. DOI: 10.1080/01431169508954424*

[58] 50° North CONTRIBUTORS. Classification accuracy assessment: Confusion matrix method, (2016), http://www.50northspatial.org/classification-accuracy-assessment-confusion-matrix-method/, accessed 03-August-2017

[59] Olesk, A., Praks, J., Antropov, O., Zalite, K., Arumäe, T. and Voormansik, K. Interferometric SAR coherence models for characterization of hemiboreal forests using TanDEM-X data. *Mdpi. Remote Sensing, (2016), Vol.8, No.9, pp.1-23. ISSN: 2072-4292. DOI:10.3390/rs8090700.*

[60] Yagüe-Martínez, N., Prats-Iraola, P., Rodriguez Gonzalez, F., Brcic, R., Shau, R., Geudtner, D., Eineder, M. and Bamler, R. Interferometric processing of Sentinel-1 TOPS data. In: *IEEE Transactions on Geoscience and Remote Sensing, (2016), Vol.54, No.4, pp.2220-2234. ISSN: 0196-2892. DOI:10.1109/TGRS.2015.2497902..*

[61] PHYS ORG CONTRIBUTORS. Sentinel-1 radar vision. Credit: ESA/ATG medialab, (2014), https://phys.org/news/2014-08-sentinel-poised-motion.html, accessed 26-Apr-2017

[62] ESA Sentinel Online CONTRIBUTORS. TOPSAR sub-swath acquisition, (2000-2017), https://sentinel.esa.int/web/sentinel/user-guides/sentinel-1-sar/acquisition-modes/interferometric-wide-swath, accessed 04-May-2017

[63] ESA Sentinel Online CONTRIBUTORS. Sentinel-1 modes, (2000-2017), https://sentinel.esa.int/web/sentinel/missions/sentinel-1/instrument-payload, accessed 04-May-2017

[64] ESA Sentinel Online CONTRIBUTORS. Level-1 interferometric wide swath SLC products, (2000-2017), https://earth.esa.int/web/sentinel/interferometric-wide-swath-slc, accessed 04-May-2017

[65] ESA Sentinel-2 CONTRIBUTORS. Introduction to Sentinel-2, http://www.esa.int/Our_ Activities/Observing_ the_ Earth/Copernicus/Sentinel-2/Introducing_ Sentinel-2, accessed 27-April-2017

[66] AIRBUS DEFENCE AND SPACE CONTRIBUTORS. Sentinel-2A satellite image, (2015), https://airbusdefenceandspace.com/newsroom/news-and-features/sentinel-2a-new-eyes-of-copernicus-ready-for-space/, accessed 27-Apr-2017

[67] ArcGIS CONTRIBUTORS. Corine land cover map description, (2017), https://www.arcgis.com/home/item.html?id=6866b2f3a44c4ee3bde8edd1b0782fb2, accessed 02-May-2017

[68] Akbari, V., Larsen, Y., P. Doulgeris, A. and Eltoft, T. The impact of terrain correction of polarimetric SAR data on glacier change detection. In: *IEEE Transactions on Geoscience and Remote Sensing Symposium (IGARSS), (2012), pp.5129-5132. ISSN: 2153-6996. DOI:10.1109/IGARSS.2012.6352456.*

[69] Antropov, O., Rauste, Y., Lönnqvist, A. and Häme, T. PolSAR mosaic normalization for improved land cover mapping. In: *IEEE Geoscience and Remote Sensing Letters, (2012), Vol.09, No.06, pp.1074-1078. ISSN: 1545-598X. DOI:10.1109/LGRS.2012.2190263.*

[70] Small, D. Flattening gamma: Radiometric terrain correction for SAR imagery. In: *IEEE Transactions on Geoscience and Remote Sensing, (2011), Vol.49, No.08, pp.3081-3093. ISSN: 0196-2892. DOI:10.1109/TGRS.2011.2120616.*

[71] Mascarenhas, N.D.A. An overview of speckle noise filtering in SAR images. In: *Image Processing Techniques, First Latino-American Seminar on Radar Remote Sensing: Proceedings of a conference held 2-4 December, 1996, Buenos Aires, Argentina,(1997), pp.71-79.*

[72] Antropov, O., Rauste, Y., Astola, H., Praks, J., Häme, T., and Hallikainen, M.T. Land cover and soil type mapping from spaceborne PolSAR data at L-band with probabilistic neural network. In: *IEEE Transactions on Geoscience and Remote Sensing, (2014), Vol.52, No.09, pp.5256-5270. DOI: 10.1109/TGRS.2013.2287712.*